ETH
Eidgenössische Technische Hochschule Zürich
Swiss Federal Institute of Technology Zurich

D ERDW
EARTH SCIENCES

Micromechanical behaviour of intact Opalinus Clay shale

Bram M.G. Vermeulen

5 October 2020

Supervisors:

Dr. Martin Ziegler
Institute of Engineering Geology, Department of Earth Sciences, ETH Zurich, main supervisor

Dr. Jakob Schwiedrzik
Swiss Federal Laboratories for Materials Science and Technology, additional supervisor

Dr. André Niemeijer
Faculty of Geosciences, Utrecht University, co-referee

Abstract

Nuclear waste needs to be safely stored for a long duration due to its long period of radioactivity. The Opalinus Clay shale formation is considered for storage of nuclear waste in Switzerland. The Opalinus Clay is an indurated clay shale with a well developed bedding and high anisotropy. When creating a nuclear waste repository, or any tunnel for that matter, the rock directly around is affected by disturbances caused by drilling and change in humidity. Cracks can form, which creates problems due to the possible leakage of radionuclides into the biosphere. Opalinus Clay contains a series of self-sealing properties, that can close fractures over time after their formation. This research is part of the SE-P project, a research project whose goal is to test in situ self-sealing processes. In this research, Vickers indentation tests at different humidity levels and at different directions with respect to bedding were done on two different sedimentary facies of intact Opalinus Clay to be able to measure changes in Young's modulus and hardness. Samples were conditioned in climate-controlled boxes with saturated salt solutions. A climatic chamber with a connection to a humidity generator was built around the test-setup to minimize change of saturation during testing. Testing and data analysis were done using the method developed by Oliver and Pharr (1992). The saturation change during tests was smaller than 4% for 98% of tests. For both hardness and stiffness a decrease was found with an increase in saturation level. Also for both stiffness and hardness, the parallel values and the sandy facies values are consistently higher than the perpendicular and shaly facies, respectively. The hardness and stiffness increase with decreasing saturation is faster for the shaly facies than for the sandy facies. For the hardness, mineralogy is the most important factor while for stiffness anisotropy is the most important. The decrease in hardness is attributed to internal bond damage due to swelling, while for the stiffness the cause of a decrease with increasing saturation is suction. The higher stiffness and hardness for tests parallel to bedding are caused by an extra strain component that is formed when stress is exerted perpendicular to bedding that is caused by the closure of microcracks. The faster decrease of stiffness and hardness of the shaly facies decreases the effect of both self-sealing processes and external damages. It also increases the damage done by swelling with each desaturation and resaturation cycle in the open drift stage.

Contents

1 Introduction

In the search for energy resources to replace oil and gas, nuclear energy is often considered. However, nuclear power plants produce nuclear waste that needs to be safely stored for a long duration due to its long period of radioactivity (up to 100,000 years). One option is to store nuclear waste underground. There are multiple rock types that are considered suitable for the storage of nuclear waste. These are generally dense rocks with a low permeability that do not allow fluids from the nuclear waste to travel to the layers around it. An example is the Onkalo project in Finland, where the repository is currently being built, and waste is planned to be stored from 2020 onwards. In Switzerland, the Opalinus Clay shale formation is considered. This rock is suitable for the storage of nuclear waste because of its low permeability and because of its self-sealing properties that allow fractures and faults to be sealed by the rock itself without human interaction.

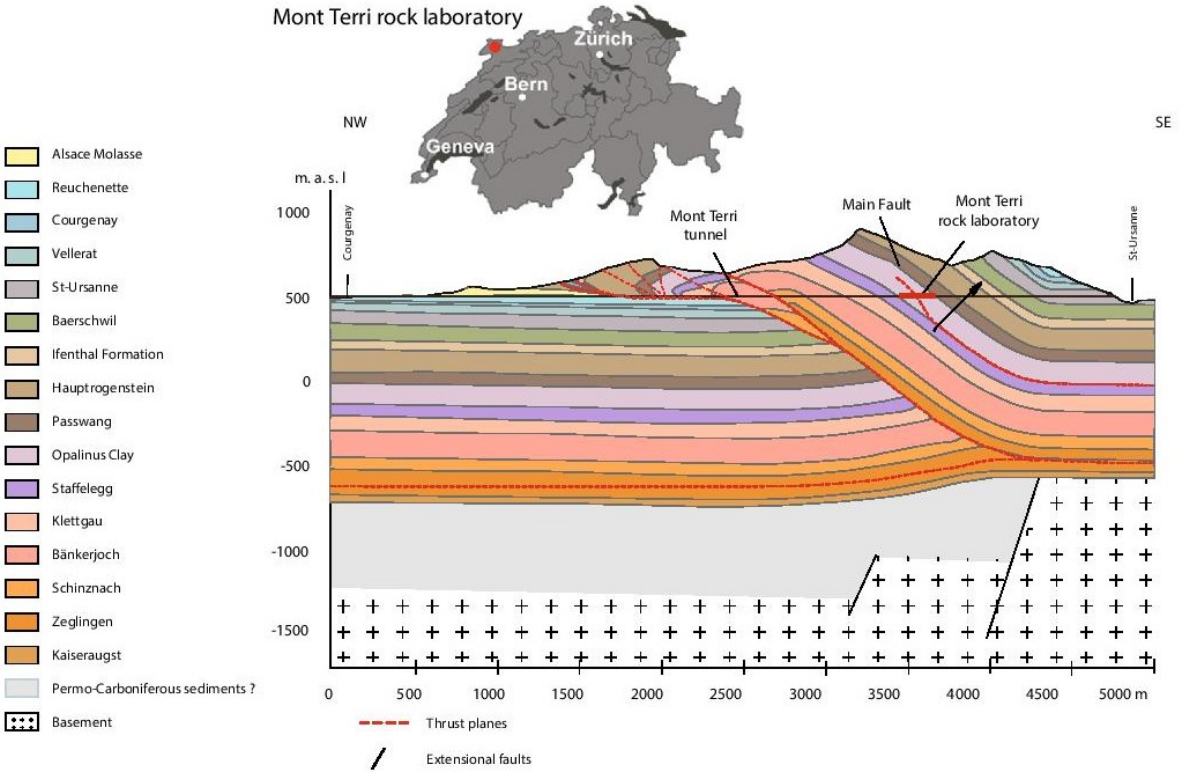

Figure 1: *Location in Switzerland of the Mont Terri underground laboratory and a cross section of Mont terri with the location of the rock laboratory in the anticline (Hostettler et al., 2018)*

1.1 Location and geology

There are not enough surface outcrops of the Opalinus Clay for it to be properly researched using only outcrops. Also, the nuclear waste will be stored in tunnels. Therefore, to research the properties and behaviour of the Opalinus Clay at depth, galleries were excavated in Mont Terri, a 804 meter high mountain in the Jura mountains in the Canton of Jura, Switzerland. The network of galleries and research facilities is called the Mont Terri underground rock laboratory (MT URL). Figure 1 shows the exact location of the MT URL, as well as a NW-SE cross-section of Mont Terri, including all formations. The Jura mountain belt is stratigraphically characterized by rocks ranging from Paleozoic to Quaternary age (Bossart et al., 2018). However, the majority of the rocks is Jurassic of age. The Jura mountains are divided into two parts (Figure 2), i.e. the folded Jura and the tabular Jura. The folded Jura is located directly to the west and

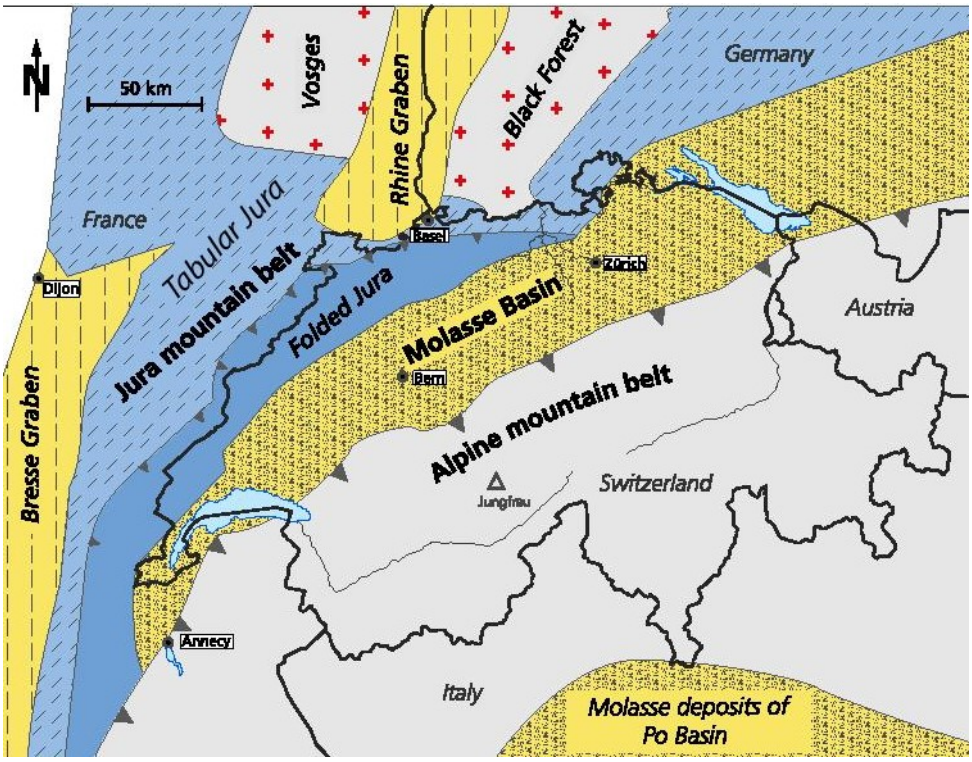

Figure 2: *Simplified geological map of the Jura mountains and its surroundings(Bossart et al., 2018)*

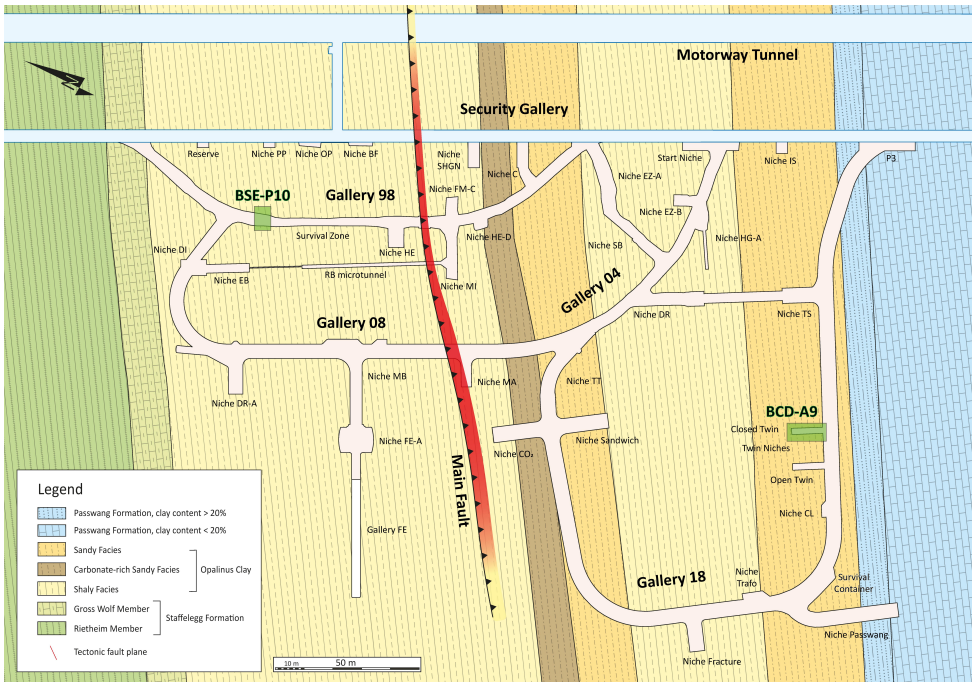

Figure 3: *Horizontal map of the MT URL with the locations at which core used for this research were drilled in translucent green.*

northwest of the molasse foreland basin of the alpine mountain belt and is a fold-and-thrust belt. The tabular Jura is located to the west and northwest of the folded Jura and is made up of undeformed Mesozoic sediments. The MT URL is located in the folded Jura. The Opalinus Clay in the area of Mont Terri exists as a 130 m thick, SE dipping layer. It cuts the MT URL at an altitude of 500 m above sealevel, at a location 300 m below the surface. At the location of

Table 1: *Difference in values for testing perpendicular and parallel to bedding for different parameters of the Opalinus Clay. The range of values is shown, with the best estimate in parenthesis. A distinction is made between the Shaly and Sandy facies. Data from Bossart et al. (2008)*

	Shaly facies		**Sandy facies**	
	Parallel wrt bedding	Normal wrt bedding	Parallel wrt bedding	Normal wrt bedding
Seismic P-wave velocity [m/s]	3170 - 3650 (3410)	2230 - 3020 (2620)	2870 - 5940 (3860)	1470 - 4610 (3280)
Uniaxial compressive strength [MPa]	4 - 17 (10.5)	5 - 10 (7)	4 - 37 (18)	6 - 37 (16)
Elastic modulus [Gpa]	6.3 - 8.1 (7.2)	2.1 - 3.5 (2.8)	2.0 - 36.7 (13.8)	0.4 - 19 (6)
Poisson's ratio [-]	0.16 - 0.32 (0.24)	0.28 - 0.38 (0.33)	0.13 - 1.23 (0.44)	0.06 - 0.42 (0.22)

Mont Terri, it outcrops in a partly eroded anticline; the Mont Terri anticline (MTA) (Figure 1). This is a non-cylindrical, domal anticline. Its northeastern border is cut by inherited sinistral strike-slip faults, and its southwestern end is interpreted as the result of cross folding (Nussbaum et al., 2018). The MT URL is located in the southeastern limb of the MTA. Figure 3 is a cross section in map view of the MT URL. The tunnel system has been expanded since the first excavations. The galleries are named after the year in which they were finished. The locations where the core used in this research were drilled are highlighted in green. BSE-P10 was drilled in the shaly facies and has therefore been used for the shaly facies tests. BCD-A9 was drilled in the sandy facies layers and therefore has been used for sandy facies tests. All core was drilled parallel to bedding.

1.2 Opalinus Clay

The Opalinus Clay is an indurated clay shale from the Toarcian to early Aalenian (approximately 174 Ma). It is the bottom part of a shallowing-upward regressive cycle known as the Liassic-Dogger units, and was formed as a deep water deposit (Blasi, 1987) that has a very well-expressed bedding. Opalinus Clay is a monotonous succession of dark grey, mica bearing clay and silty marl, with carbonate and sandy lenses that become more abundant towards the top (Bossart et al., 2018). Clay platelets are tabular-shaped and lie sub-parallel with the macroscopic bedding, which is made up of siderite concretions and silt and sandstone lenses. The porosity from water loss of the shaly facies varies between approximately 13–20% (Wild et al., 2015). The anisotropy is seen in many rock properties that are different when measured parallel or normal to bedding. Finally, in situ the Opalinus Clay is 100% saturated.

1.2.1 Mineralogy

Opalinus Clay is mainly made up of the clay minerals illite, chlorite and kaolinite and mixed layers of illite and smectite (Table 2). Further components include quartz, carbonates, feldspars, pyrite, organic matter and accessory minerals. The Opalinus Clay is up to 150 m thick (Bossart et al., 2018) and the relative amount of each mineral is not the same throughout the formation. Therefore, the Opalinus Clay has been divided into three facies; a shaly facies, a sandy facies and a carbonate rich sandy facies. The shaly facies is relatively richer in illite, chlorite, kaolinite and smectite while the sandy facies contains relatively more quartz and the carbonate rich sandy facies contains relatively more carbonate material. The three facies are made up of five layers arranged from bottom to top: shaly, sandy, carbonate, shaly and sandy facies (Bossart et al., 2018). So there are 5 layers but only three defined facies. Table 2 contains the proportions of different minerals in the facies in weight percent.

Table 2: *Table of mineralogical components of different facies of Opalinus Clay based on Bossart et al. (2018)*

Mineralogy	Shaly facies (wt%)	Sandy facies (wt%)	Carbonate-rich sandy facies (wt%)
Clay minerals			
Illite, chlorite, kaolinite	39 – 80	29 – 70	8 – 45
Illite/smectite mixed-layers	5 – 20	5 – 15	3 – 8
Quartz	10 – 27	22 – 44	22 – 36
Carbonates			
Calcite, dolomite, aragonite, ankerite, siderite	4 – 35	11 – 25	34 – 57
Feldspars			
Albite, K-feldspar	0.3 – 5	0.2 – 6	3 – 11
Pyrite	0.9 – 1.4	1 – 1.2	0.2 – 0.5
Organic matter	0.8 – 1.4	–	–
Accessory minerals			
Apatite, celestine, zircon, monazite	<0.1	<0.1	<0.1

1.3 Excavation damage zone and repository process

To be able to place the waste in the repositories, excavation activities need to take place that disturb the rock around the repository. Because of this, perturbations of boundary conditions (saturation, temperature, stress, pore pressure, etc.) will be induced (Marschall et al., 2018). The zone where these changes occur is called the Excavation disturbed Zone (EdZ). A certain part closest to the tunnel wall can be disturbed so severely, that it might show damage in the form of cracks and fractures. This part of the EdZ shows damage, which is why it is called the Excavation Damaged Zone (EDZ). The EDZ can create problems for the storage of nuclear waste because cracks can easily form inside of it, and the permeability might be increased because of this. An initial increase in permeability of five orders of magnitude has been measured at Mont Terri (Tsang et al., 2012). Increased permeability increases the danger of radionuclides reaching the biosphere through the weakened rock of the EDZ. According to Tsang et al. (2005), the changes that the rock in the EDZ goes through can be divided into four stages.

First the construction stage, which involves the period between start of construction to the installation of liner on the tunnel walls. During the excavation of any URL, it is necessary to evaluate what support is needed to avoid collapse of the tunnels. For the MT URL, this is a 10-15 cm thick shotcrete (a wet concrete that is sprayed against the wall) (Tsang et al., 2012). During this stage, the region adjacent to the tunnel wall is able to change from water saturated to unsaturated conditions. This can have an effect on the rock behaviour, making it more brittle when it is less saturated (Delage et al., 2007). The open drift stage is the period between completion of excavation and emplacement of waste. During this stage, the rock closest to the tunnel wall is exposed to the tunnel atmosphere for months to years. Temperature changes and tunnel ventilation may influence the rock properties, because desaturation may be caused. Desaturation creates capillary forces and with that increases rock strengthening and cohesion. Furthermore, it might also increase tensile stress and the potential for bond failure (Tsang et al., 2012). During the open drift stage, seasonal varieties in temperature and humidity may change the rock saturation. When humidity is increased, rock softening and swelling may occur in the rock closest to the tunnel wall. Clay swelling might increase compressed stress, which leads to additional damage to the softened rock. The third period is the exploitation stage, which indicates the start of decay heat generated by the radioactive waste During the exploitation

stage the repositories are backfilled with bentonite, which is a natural clay mixture that consist of mostly montmorillonite of hydrothermally altered, volcanic origin. This stage is ended by the closure of the repository. During the exploitation stage resaturation occurs. However, this does not happen uniformly over the repository domain. The heating will cause steam convection and transient pore-pressure buildup that result in differential thermal expansion, which in turn leads to changes in effective stress. Finally, the long term postclosure stage is the period from sealing of the tunnels. At this stage the long-term geochemical processes become important. For example, corrosion and degradation of concrete lining, canister steel and steel supports become more important. This is also the part where self-sealing process are most important (Section 1.4). The processes and effects that occur during the first three stages influence the characteristics of the rock in the long term. These long term characteristics are important for the transport behaviour of the radionuclides that release from the waste canisters in the fourth fase.

1.4 Self-sealing properties

The Opalinus Clay contains properties that allow it to close the cracks created by the aforementioned processes itself. For this whole section, Bock et al. (2010) was used as a basis. There are four different types of self-sealing processes important to this research. 1) Material compaction: The clay platelets themselves are not compressible, but the framework of platelets as a whole is deformable when subjected to external and/or internal loads. The shape and volume of the framework's voids might be changed by this, affecting the fluid flow characteristics of the material. For deep geological repositories, this is of limited importance, because the considered material has already been geologically precompacted so much that diffusion instead of advection has become the dominating mass transport mechanism. 2) Physico-chemical processes within the microscopic pore space: Rock excavation causes mechanical unloading which leads to thermodynamic disequilibrium in both the solid and liquid phases. Fracturing along the clay platelets will promote a permeability increase. This is counteracted by two processes: swelling and slaking. Swelling is a time-dependent process where free water is drawn into the material resulting in a volume increase. Swelling can be caused by stress relief. There are three processes that can induce swelling on the microscale: a) In argillaceous material, exchangeable cations that are positioned at the inner surfaces of clay minerals are hydrated. An example is smectites, where the spacing between adjacent clay platelets can be increased to a multiple of the original distance. Water absorption occurs at free lamellae surfaces and osmotic swelling due to the adsorption of water in between clay lamellae (Nüesch, 1991). b) Isomorphous substitution of aluminium or silicon atoms of lower valence create negative charges at the outside of clay particles. Water reacts with them and form hydrogen bonds with the silicate oxygen. Eventually, free energy of water is reduced and water adsorption and swelling occur until the activity or chemical potential of associated water becomes equal to that of free water (Wong and Wang, 1997). c) A double diffusive layer is formed by the association of negatively charged clay particle surfaces with positively charged layers of dispersed cations. An osmotic pressure is subsequently created by the interaction of two differently charged layers. Inward migration of water into the intramatrix pores can then change the osmotic pressure and create swelling. After this an equilibrium is reached with a permeability that is equal or similar to the original situation (Mitchell, 1993).

3) Surface slaking, sedimentation and clogging of fractures: Slaking occurs when clay particles repulse each other due to the expansion of double layers. The diagenetic bonds between the particles can break when the repulsion is large enough. When this happens in a fracture wall the particles will be dispersed into the fracture space. This can seal the fracture space over a large volume. 4) Precipitation of minerals: There are major faults in the Opalinus Clay in both Mont Terri and the Molasse Basin (Figure 2). These structures contain no or very

minor mineralisation, indicating that since the creation of the faults, very little to no fluid flow along these structures has occurred. There are two pysico-chemical processes that can lead to precipitation of minerals in the fractures in the EDZ. The first one is by evaporation in the rock located closest to the tunnel. The ventilation of the repository desaturates the rock and by doing so solutes are transported towards the tunnel wall by capillary-driven advection. These can create minerals that close the fractures The second type is by oxidation. In a rock like the Opalinus Clay, the only relevant oxidation process is that of pyrite (Table 2), which forms sulphuric acid when oxidised. When sulphuric acid reacts with the calcite that also occurs in the Opalinus Clay it forms gypsum which can also close the fractures. For many of these self-sealing processes the water content (saturation) of the rock is important because the desaturation can change the rock properties significantly. This is also why in this research the difference in properties between different saturation levels will be addressed. Note that the self-sealing processes are most active in the illite/smectite mixed layers (Table 2). The facies of Opalinus Clay that are researched most are the shaly and sandy facies because they have the highest weight percentage of illite/smectite mixed layers.

1.5 Previous work

Table 3: *Basic properties of the Callo-Oxfordian and shales (Niandou, 1994; Niandou et al., 1997; Schmitt et al., 1994; Zhang and Rothfuchs, 2004; Chiarelli et al., 2003; Brown, 1981; Mäder et al., 2014; Bock, 2001)*

	Callo-Oxfordian	Opalinus
Bulk density [g/cm^3]	2.38 - 2.41	2.4 - 2.53
Dry density [g/cm^3]	2.18 - 2.27	2.28 - 2.32
Water content [saturated wt%]	4.0 - 9.0	5.0 - 9.8
Total physical porosity [vol%]	11.0 - 15.0	14.0 - 24.7

Auvray et al. (2017) performed nano- and microindentation tests and macro-compression tests on the Toarcian Callovo Oxfordian claystone, using a similar method as in this research. The method by Oliver and Pharr (1992) was also used. The tests were done using a maximum displacement instead of a maximum force. The loading and unloading rate for the micro-indentation tests was 30 N/min and measurement of the elastic modulus occured at a constant depth of 20 µm. This claystone is composed of 55% clay, 19% quartz, 12% feldspars/mica, 3% sulphides (pyrite), 10% carbonates and 1% kerogen (Niandou, 1994; Schmitt et al., 1994; Niandou et al., 1997; Charpentier et al., 2001; Tinseau et al., 2006; Savoye et al., 2008), and as such contains a similar composition as the shaly facies of the Opalinus Clay (Table 2). Table 3 displays some important properties of the two clay shales. This shows that these are as well similar to each other. In the these experiments, micro-indentation tests were only done perpendicular to bedding and at a saturation of 30%. The results for the elastic modulus were extremely scattered, with values ranging between 20 - 60 GPa with two peaks located around 26 and 37 GPa. Nano-indentation and meso-compression tests were also done for this material. For the nano-indentation tests the elastic modulus distribuiton shows an even wider spread from 15-90 GPa with two large peaks, while the meso-compression tests have a tighter elastic modulus, ranging from 25-50 GPa and only one peak. According to the author, the wide spread is caused by the existence of three families that probably represent the modulus values for a matrix of variable purity, a matrix containing variable numbers of micro-inclusions and for zones containing little matrix and variable numbers of inclusions. The difference in spread size for different scales can be explained by the fact that the heterogeneity is larger at the small scale than at large scale in rocks like these.

This means a spread like this might occur in this experiment as well, because the same heterogeneity may very well be present in it. To counteract this problem, a very large data had to be created. Because of this, a set of approximately 90 tests per saturation level and direction were done so that statistically there should be trends between different saturation levels. Bossart (2011) gives a Young's modulus on the sample scale of 7100 - 11900 MPa perpendicular to bedding and 11500 - 19500 MPa parallel to bedding. These values and the fact that the Young's modulus is higher parallel to bedding than perpendicular to bedding can be expected in this research as well.

Wild et al. (2015) researched the change in rock properties due to a change in suction. The conditioning was done using the same method as presented in this research. The properties are tested here on the macroscale. The saturation was also changed by placing samples in a climatic chamber for a period of time until they were in equilibrium. A lower saturation equals a higher suction. One interesting aspect about the acclimatisation of the samples is that not all climatic boxes reached the theoretical relative humidity. As such, it can be expected that in this research not the exact humidity levels mentioned in Table 4 will be reached. The experiments done resulted in a very fast, linear increase in Young's modulus for suction between 0 and 56.6 MPa (approximately 100 - 64% saturation). After this, E did not increase any further. For Poisson's ratio the opposite is true. The P-wave velocity did not vary much with increased suction. This might be caused by the fact that the Young's modulus increases while the Poisson's ratio decreases and they have opposing effects on the P-wave velocity. Due to the similarity of the rock and the test method, similar results as in Wild et al. (2015) can be expected.

Ojo and Brook (1990) used a shore scleroscope test on a sandstone. Here the hardness is measured by using a diamond-tipped hammer that falls from a known height. The hardness number is based on the heigh to which the hammer rebounds. The samples were saturated to 100% and then left to dry, while measuring the scleroscope hardness. For a degree of saturation of 100%, the hardness is 14.85, while it is 29.40 for a degree of saturation of 9.1%. The hardness increases with decreasing saturation levels. Michalopoulos and Triandafilidis (1976) performed a similar research on eight different kinds of rocks, but measuring indentation hardness. They also concluded that indentation hardness increases with decreasing saturation. They relate this to the effects that water might produce in weakening the bond strength of the rock structure irrespective of the pore-water pressures generated.

Sone and Zoback (2013) used various shale-gas reservoir rocks that were prepared perpendicular and parallel to the bedding planes. They were then pressurized in a servocontrolled triaxial deformation apparatus to observe its static and dynamic elastic properties and creep behaviour. The sample deformation parallel to bedding was measured by a pair of differential transformer displacement transducers and the deformation perpendicular to bedding by spring-mounted strain-gauge transducers. They concluded that there was more viscoplastic creep in samples deformed perpendicular to the bedding than parallel to bedding. The creep tendency also correlated with the static young's modulus, which is something that could be expected in this research as well. The correlation between creep and Young's modulus is explained with the stress partitioning that occurs between the stiff components (feldspar, quartz, pyrite) and the soft components (clay and kerogen).

Finally, Ping et al. (2015) performed microindentation tests on shale outcrop samples from the Camrian Longmaxi Formation in the Changning area, Sichuan Basin, China. The loading range used was between 0.5 - 50 N with a loading rate of 15 N/min with a Berkovich indenter. The authors conclude that at a maximum load of 75 N or 100 N, cracks or even major breaking occurs. Therefore, in this research no higher force than 50 N will be used as well. This is not

a clay shale, but a shale with average content of quartz, calcite, dolomite and pyrite of 43.4%, 20.6%, 16.8% and 1.4% respectively. The distance taken between two indentations was 20 times the indentation depth. Indentation hardness varied from 0.18 to 3.61 GPa, and varied much for different compositions and densities. The elastic modulus gave a normal distribution, with peak ranging from 20-23 GPa, and a minimum of approximately 7 GPa and approximate maximum of 40 GPa.

1.6 Research goals

This research is part of the SE-P project; a research project about self-sealing processes in excavation damaged zones at the Mont Terri URL. In the context of the SE-P project, a lot of work has been done on researching the mechanical behaviour of the Opalinus Clay. However, most of this research has been done on the macroscale. In the SE-P project, systematic water content measurements are taken to assess the variation in rock saturation in situ. This is done because Saturation and desaturation may lead to formation of microcracks, mineral precipitation, or swelling / shrinkage (Williams et al., 2019).
These are all processes that occur on the microscale. Therefore we research the hardness and elasticity (Young's modulus) of the material on the microscale. The tests will be done with variations in the saturation, rock facies and direction with respect to the bedding. The saturation is changed to research what exactly the effect of this is on the micromechanical properties and behaviour because the saturation will also change due to the processes explained in Subsection 1.3. The research questions to be answered are

- What is the effect of saturation on the microscale stiffness and hardness of Opalinus Clay shale
- What is the difference of the effect of saturation on hardness and stiffness for different facies (shaly, sandy) with different mineralogy?
- What is the difference in hardness and stiffness when tested in different directions with respect to the bedding and how do changes in saturation affect this?
- How can changes in micromechanical rock properties due to humidity changes effect the sealing of fractures?
- How do hardness and stiffness differ between the micro- and macroscale?

2 Indentation tests

2.1 Hardness tests

The hardness of a solid material is defined as a measure of its resistance to a permanent shape change when a constant compressive force is applied (Broitman, 2017). The permanent shape change can be made by different mechanisms, like bending, cutting, scratching or indentation. In this experiment, indentation testing was used to analyse the hardness of the material. In indentation hardness testing, an indenter is pushed into the material at a certain loading rate (N/s) until a certain force is reached. The indenter will then stay at the maximum force for a certain period of time, after which it is unloaded. The applied force and the loading rate can be chosen based on the material and the kind of desired data. The created strain will differ between experiments and is dependent on the material and the test type. With a microscope the dimensions of the indentation can be measured and the hardness can be derived from either the depth of the indenter penetration or the size of the impression, dependent on the kind of hardness test.
There are three main types of indentation testing, dependent on the amount of force that is exerted on the material and the size of the indenter. In macroindentation tests, the indentation load is anywhere between 2 KN to 30 KN, while in microindentation, the load is smaller than 2 KN. In nanoindentation the load is also smaller than 2 KN but the indenter is so small that the properties of individual grains or inclusions can be measured. Because we want to test the micromechanical properties of the material, we have used microindentation tests. There are two main microindentation tests (Section 2.2).

2.2 Microindentation tests

2.2.1 Vickers test

The Vickers hardness test can be used for both micro-and macroindentation. The macro version was created in the 1920s by Smith and Sandly (1922), while the first microindentation Vickers tests were done by Lips and Sack (1936). The indenter is a square-based pyramid whose opposite sides meet at the apex (the point where all sides come together) with an angle of 136°. This means that this will also be the aproximate angle created in the indentation. The time for initial application of the force is 2-8 s, and the test force is maintained during 10-15 s. The diagonal length d (Figure 4) should be larger than 0.020 mm and smaller than 1.4 mm. The thickness of the test piece should be at least 1.5 times the diagonal length d. The depth of the indenter and with that the indentation is approximately one seventh of the diagonal length (0.143d), which means the maximum depth of the indentation is $0.143 \cdot 1.4 = 0.2002$ mm and the minimum depth of indentation is $0.143 \cdot 0.02 = 0.00286$ (ISO-Standards, 2005) (E92-16, 2016).
In this test, the Vickers diamond hardness number (HV) is calculated from the indenter load (L) in kg and the actual surface area of the impression (A_c) in mm^2:

$$HV = \frac{L}{A_c} = \frac{2L}{d^2} \sin \frac{136^\circ}{2} = 1.8544 \frac{L}{d^2} \tag{1}$$

Using Equation 1, only the distance between two opposite points in the impression (d) needs to be known along with the applied load to calculate the hardness number (Figure 4). The Vickers hardness is reported in kg/mm^2. This can be converted to Newton by multiplying it by 9.8065 (the gravitational constant).

2.2.2 Knoop test

The Knoop test is similar to the Vickers test, but a different kind of indenter is used, and therefore the formula used to calulate the indentation hardness is different as well. For Knoop

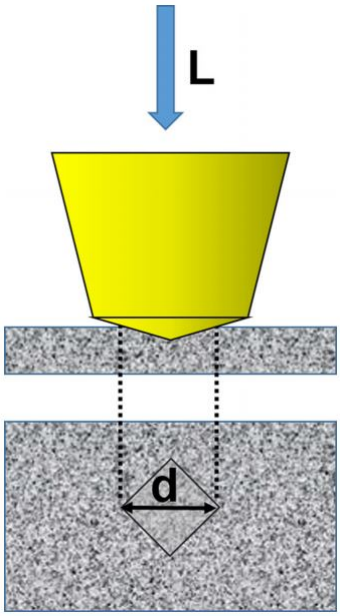

Figure 4: *Vickers microindentation test where L is the applied load in kg and d is the distance from corner to corner on the impression in the specimen surface in mm (Broitman, 2017)*

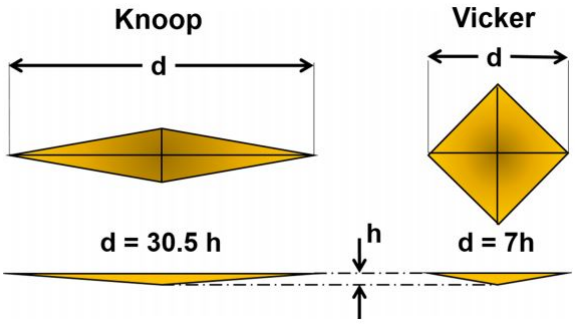

Figure 5: *Schematic representation of the difference between the Knoop and Vickers microindentation tests. Top is the view from above of the microindentation made and below is a section of the indentation from the side. d represents in both cases the length to be used to calculate the indentation hardness while h is the height difference between the original surface and the depth of the indentation. (Broitman, 2017)*

.

tests, a rhombic-based pyramidal diamond indenter is used that produces an elongated diamond shaped indent. The angles from the opposite faces of the indenter are 130°and 172.5 °(Knoop et al., 1939). Figure 5 demonstrates the difference between the indenters used for the Knoop and Vickers microindentation tests. The Knoop hardness number (KHN) is defined as the ratio of the applied load (L) divided by the projected area (A_p) of the indentation.

$$KHN = \frac{L}{A_p} = \frac{2L}{d^2[cot\frac{172.5^\circ}{2}tan\frac{130^\circ}{2}]} = 14.24\frac{L}{d^2} \tag{2}$$

where d is the length of the longest diagonal in mm. Here L is also measured in kg and the load should be maintained for 10-15 s (E92-16, 2016). For our experiments the Vickers indenter was used because the required calculations are independent of the size of the indenter, and the indenter can be used for all materials irrespective of hardness (E92-16, 2016).

3 Sample preparation

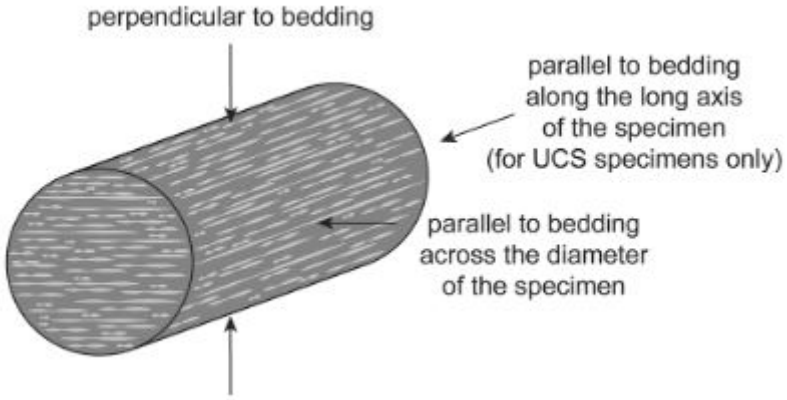

Figure 6: *direction of bedding with respect to the core (Wild et al., 2015)*

3.1 Cutting

The researched cores were drilled from the Mont Terri underground rock laboratory in the locations indicated in Figure 3. These cores were drilled so that the long side of the core is parallel to the bedding, so that a slab that is cut off can be tested parallel and perpendicular to bedding without having to cut slabs oblique to the cylinder (Figure 6). The cores were then stored and vacuum-sealed in aluminium foil bags and a PVC liner with resin filling of the gaps at the ends of the cores. The test surface of the samples may not be larger than 17x17 mm because the samples were placed on a round sample holder (Section 3.2) with a diameter of 25 mm. To be certain that the samples do not overlap the surface of the sample holders, the samples were cut so that the test surface is 16x16 mm. The samples were then polished in a steel polishing device (Section 3.2) with a distance between the bottom and the place where the polishing is cut off is 9 mm. The samples were cut from the slabs so that samples with a thickness of 10 mm were created. Then, 1 mm of rock was polished off using the polishing device so that a 16x16x9 mm sample is created with a flat, smooth surface. This means that the samples were all cut to 16x16x10 mm. However, the manner in which they are cut was different for the samples that were tested parallel to bedding compared to the samples that were tested perpendicular to bedding. For the samples created for testing parallel to the bedding, the thickness of 10 mm is the amount of core that is cut off, because the side that will be tested is the side that is named "parallel to bedding along the long axis of the specimen" in Figure 6. The samples that were cut perpendicular to bedding, will be tested like indicated by the arrow in Figure 6 that indicates "perpendicular to bedding". For these samples, the amount of core that needs to be cut to create them is 16 mm. This means that slabs of core of 16 mm and 10 mm were cut. From the 10 mm thick slabs that are used for testing parallel to bedding, 6 samples can be cut while for the 16 mm thick slabs, 10 samples can be cut (Figure 7). The cores were first cut in slabs of 16 and 10 mm with a Marpol Model 95 bandsaw. The slabs were then taped and vacuum sealed in a plastic vacuum bag using a standard kitchen grade vacuum packing machine to make sure no air could reach the sample and to prevent it from desaturating. Then, the slabs were unpacked and cut into samples using a Proxxon MBS 240/E saw. The samples are cut like aforementioned and illustrated in Figure 7.

For both directions with respect to bedding, the samples were tested at six different humidity levels, and for each combination of bedding direction and humidity level, six samples are needed.

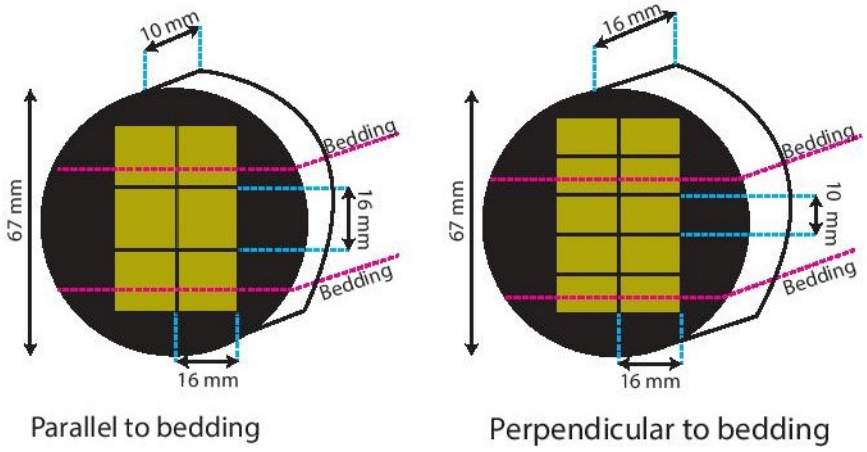

Figure 7: *Schematic view of how the samples are cut out of slabs of core for samples parallel and perpendicular to bedding.*

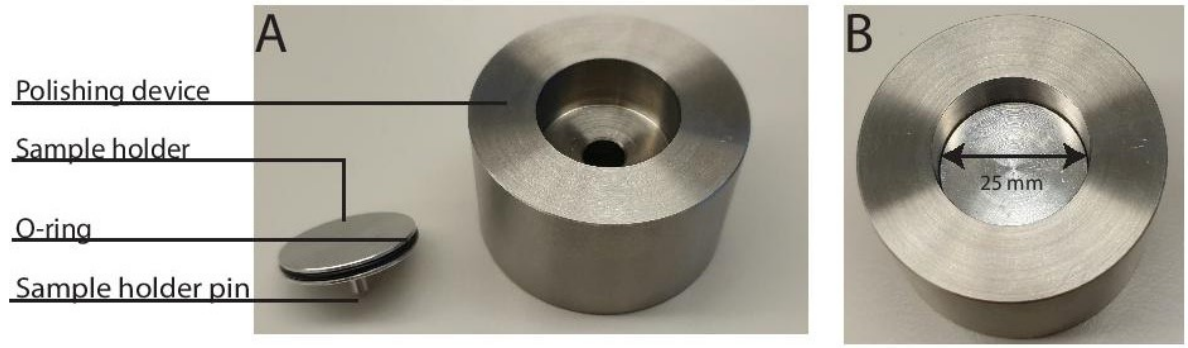

Figure 8: *A: The sample holder with o-ring on the left and the polishing device on the right. The pin in the bottom of the sample holder fits in the hole in the polishing device. B: The sample holder in the polishing device. Normally the sample would be glued to the sample holder in this situation.*

Three samples is enough to obtain statistically significant results. However, the eventual amount of samples cut was between 6 and 10 per combination of saturation, direction to bedding and facies. This is because many problems occured regarding the glue and the stability of the samples at higher humidities.

3.2 Polishing

After the cutting, the samples were taken out of their plastic vacuum bags and glued onto a round 25 cm sample holder with a pin in the bottom that is used for holding the sample during the test. Three different types of glue were used. Firstly UHU endfest, secondly UHU sekundenkleber and finally UHU alleskleber. The reason three different types of glue were used is that neither of them worked at high humidity (>90%). The glue would not stick between the sample and the holder, but create a crust that would make the sample fall of the holder. For further experiments using this method, using a different glue than the aforementioned ones is advised. For the humidity levels between 15% and 85% the UHU endfest worked in most instances. When the glue had dried the sample holder and sample were placed into a cylindrical metal holder (polishing device) that can hold the sample holder with sample perfectly (Figure 8). As mentioned, the sample thickness of 10 mm is just enough for the sample to stick out above the polishing device with 1 mm so that it can be polished off. The purpose of the polishing is to smoothen out any irregularities created by the saw cutting, and to make sure that the test surface is straight. This creates a higher certainty that all tests are performed on a similar surface. The polishing was done manually because electric polishers would break the samples

of the holders as the glue was not strong enough. The sandpaper used had a grit of 240 (3M standard), which is considered a fine grit.

3.3 Conditioning

The samples needed to be conditioned to different saturations in order to be able to make indentations at different saturation levels. Oversaturated salt solutions in climate-controlled boxes were used to achieve this. The climate-controlled boxes are plastic boxes with a cover to close it off and a fan to keep the air inside the box moving. The saturated salt solution was placed in an open plastic container with large surface area at the bottom of the climate-controlled box with a metal rack placed over it to place the samples on. The samples were not placed directly on the metal rack but in plastic cylindrical containers with a hole in them. The pins of the sample holders fit tightly in the holes in the containers. This made it easier to weigh the samples, as the sample and sample holder could stay upright. The lid of the containers was left off so that the controlled-humidity air could reach the samples. According to Young (1967), there are five important points to follow when you want to condition samples using salt solutions so that equilibrium will be reached as efficiently as possible: 1) The chamber and anything in it should be made of non-hygroscopic materials (except for the salt itself) to prevent adsorption of moisture by the walls, which could lead to delay in achieving equilibrium. 2) The chamber should be leak proof. 3) The temperature should be kept constant. 4) The salt solutions should have a large surface area. 5) The air should be circulated and the fan motor should be mounted outside the chamber to avoid internal heating. The boxes were stored in the rock mechanics lab at ETH department of earth sciences where the temperature is normally between 20-25°C, wich is a sufficiently small temperature range to make sure it has no effect on the efficiency of the salt solutions. This means that these five points have been accounted for.

Six humidity levels were chosen for the acclimatisation of the samples. Table 4 contains the expected humidity levels for the different salt solutions, the salts used to achieve these humidity levels and the solubility at 20°C. The last column is the actual humidity measured inside the boxes. It is assumed that this is the level that the samples were saturated to. Note that if the quantity of salt in Table 4 is added to 100 ml, it all dissolves eventually. Subsequently, the desired humidity is reached for a moment but eventually changes. That is why the salt solutions were oversaturated, so that there were always visible salt crystals in the water. 200 ml of water was used so the amount of salt needed to establish the desired humidity level is twice the amount in Table 4. Another approximately 25% of the amount of salt needed to saturate a 100 ml solution was added to make sure the solution would stay oversaturated for a period long enough to reach equilibrium. While they were being conditioned, the samples had already been glued to the sample holders and polished. Together they were weighed using a high precision (down to micrograms) scale just before being placed in the climate-controlled box. Following this, from every box samples were weighed every day. The weighing was done quickly so that the samples were exposed to the room air as shortly as possible. The samples were at the desired saturation level when the weight of the samples remains equal for two days in a row. For this method it is assumed that the glue does not take on or lose moisture during the process. Xiaomi relative humidity and temperature sensors were used to measure the humidity in the climate-controlled boxes. The sensors were first all tested in the same climate-controlled box to make sure whether any corrections are needed. The humidity levels are not equally divided over the spectrum. Four out of six humidity levels are 60 percent or higher. This is because the humidity in a real nuclear repository would not go below 60% either, also not during the open drift stage. The lower values were chosen to be able to gain knowledge on the full spectrum, but the higher humidity levels are more realistic.

Table 4: *Intended relative humidity levels and salt solutions used. The fifth column contains the humidity levels measured in the boxes.*

Salt solution	Temperature (°C)	Solubility at 20°C (g/100ml H2O)	Rel. humidity(%)	Achieved humidity (%)
Potassium sulfate	20 - 25	11.6	97	99.9
Potassium chloride	20 - 25	34.4	84	85
Sodium chloride	20 - 25	36.0	75	76
Sodium bromide	20 - 25	90.6	58	60
Potassium carbonate	20 - 25	110.6	43	45
Lithium chloride	20 - 25	81.9	15	13

4 Experiments

4.1 Indentation tests

4.1.1 Test set-up

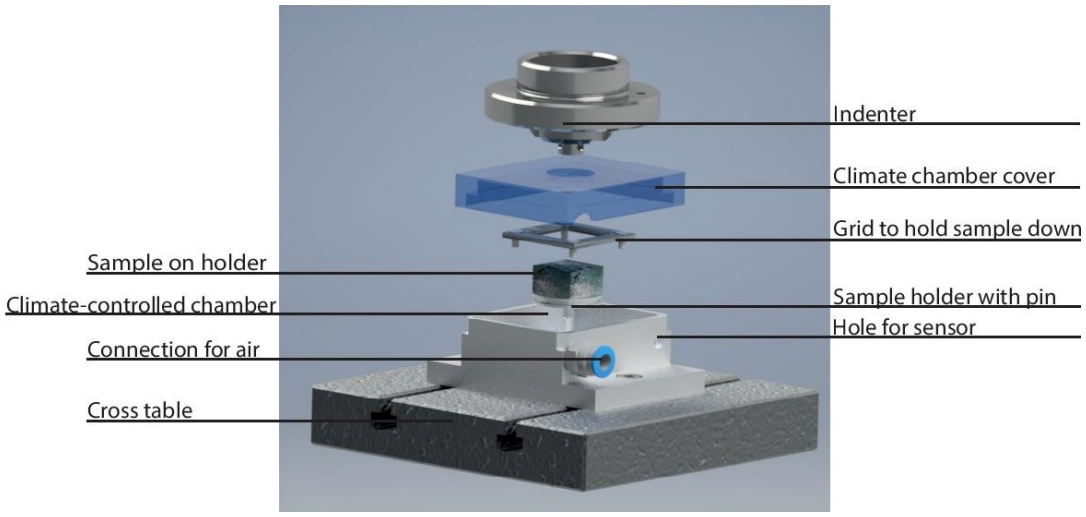

Figure 9: *Test set-up drawing. In this impression the cover with the 15 mm round hole is used.*

Figure 9 is a schematic view of the test set-up. The base of the test setup is a 238x146x18 mm metal plate (not in the drawing) that is used as an intermediate between the cross table and the indentation device. The attachment between the base plate and the crosshead of the indentation device is through two screws. The cross table is attached to the base plate with two stud bolts. The cross table is a 135x135x72 mm metal device that consists of three parts. The bottom part is the base that is used to screw the device to the base plate. The other two parts are mobile. One slides in the x-direction and the other one in the y direction. Both parts can traverse for a distance of 25 mm and have a minimum scale distribution of 10 μm. This creates a grid of 2500x2500 points where the cross table can be placed. Both parts contain a measuring screw that is used to place the part at an exact location. Finally, the upper part contains two gliding slots at the top for attaching the climate-controlled chamber.

The climate-controlled chamber is a box made of stainless steel. Its function is to hold air with a specific humidity, equal to the saturation the sample was conditioned to around the sample so that the humidity stays controlled and the sample is not able to interact with the air in the room. The climate-controlled chamber is sealed off by a cover with a round hole with a diameter of 25 mm in the top so that switching is possible between the indentation device and the microscope. To do this the indentation device needs to be lifted up automatically using a computer that is connected to it, then moved to the side so the microscope lens is above the sample, and moved back down again, or vice versa. The hole also allows for the indenter to move inside the hole. Two different covers were used for different humidities, because high humidities could not be achieved due to the large hole (Section 4.1.2) At one of the sides of the climate-controlled chamber holes are present to accommodate the air hose and humidity/temperature sensor. The Sample holder with sample attached to it fits in the climate controlled chamber with the pin in the bottom of the holder. The sample is held in its place by a metal grid that is screwed in the climate-controlled chamber. The indentation device is a Zwick BZ2.5 micromechanical indenter. Apart from the test set-up a computer for data acquisition and the Setaram Wetsys humidity controller were situated on the same table. The vibrations of the computer and the Setaram Wetsys were not of sufficient magnitude to influence the outcome of the tests. However, activities like typing were

avoided during active tests in order to exclude the influence from outside movements on the test results. The controlled-humidity air comes from a Setaram Wetsys controlled humidity device that was connected to a pressurised air connection using a pressure of 3 bar. The Wetsys can create a maximum internal relative humidity of 95%, a maximum internal water temperature of 80 °C and a flow rate of 200 ml/min. Using the highest of these three settings an external humidity (in the climate controlled chamber) of 98% can be achieved.

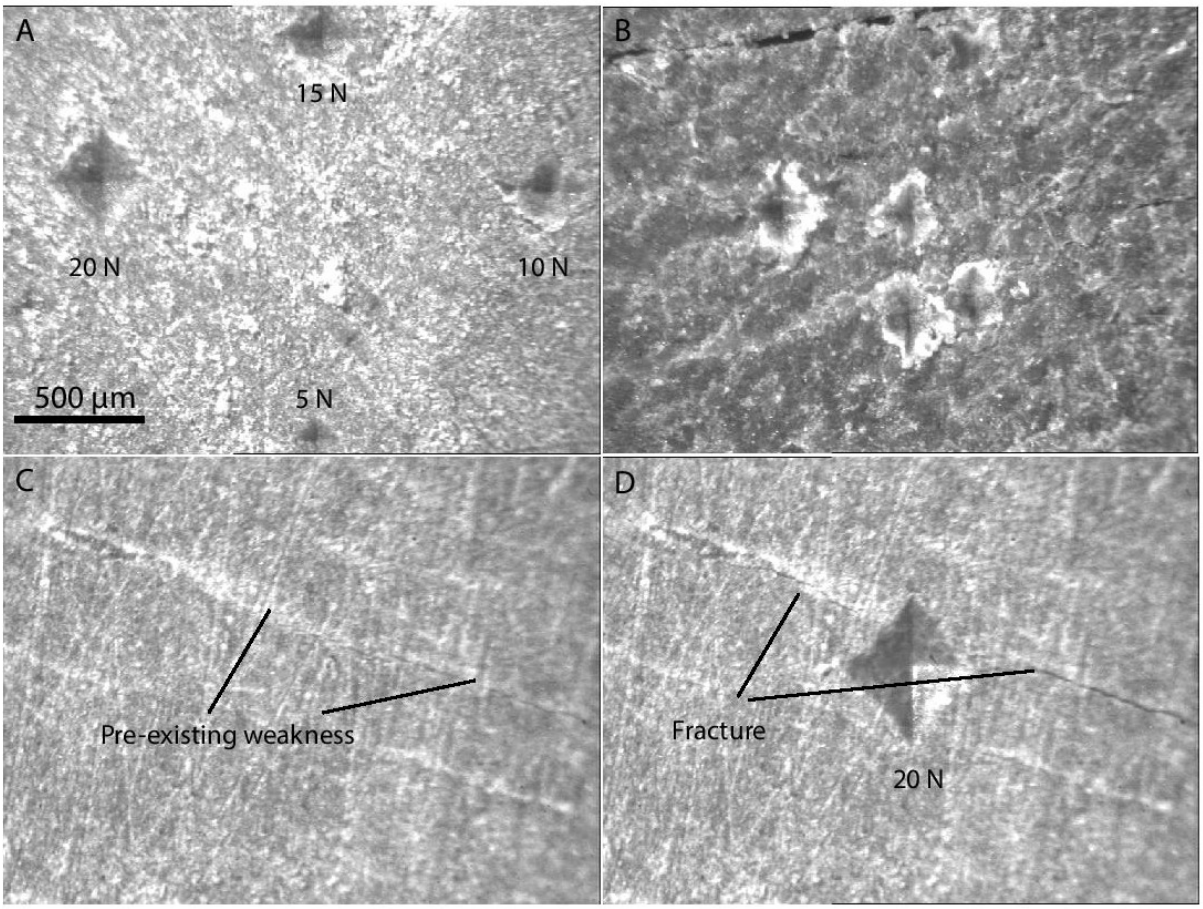

Figure 10: *Microscope pictures of indents. A: Four indents made at different maximum forces. B: Indents made in the top layer that has experienced deposition of minerals on the surface. C: A pre-existing weakness on the surface of a rock sample. D: A fracture has formed at the location of the pre-existing weakness following an indentation at 20 N.*

4.1.2 Preparation

Baseline tests were performed in order to determine the force to be used in the eventual tests. If the force is too small, the indents become too small to measure or see under the microscope. When the force is too large, the experiments can damage the rock and create unusable results. Also, the depth of the indent should be larger than 0.02 µm because indents below that value are in the nano-indentation range. Figure 10 shows the results of this baseline testing. In Figure 10A, four different forces were used for indentation testing. It is clear that the indents become larger with larger force, and therefore are also easier to see and measure. However, Figure 10C and D show that at a force of 20 N, pre-existing weaknesses can become fractures due to the applied force. This was not observed for indents made at forces of 15 N and lower. Eventually a maximum force of 15 N was chosen for these experiment The indentations leave a mark in the rock that affects the material directly around the indentation itself. Therefore, a set distance between two indentations needs to be taken into account to make sure no indents are made in a

part of the rock that has been affected by another test. The same distance needs to be used for the distance between the edge of the sample and the indentations closest to the edge. According to Phani and Oliver (2019), a spacing of 1.5 times the diagonal of the indent (d in Figure 5) between two indentations is sufficient to obtain accurate results. The indents made at 15 N have a depth between 40 and 120 µm and a diameter between 280 and 850 µm, which means that a distance between two indents should be at least 1.3 mm. A distance of 2 mm between the center of two indents was used in these experiments. The same distance is taken between the indentations closest to the edge of the sample and the edge itself. Figure 10B shows what happens to some samples when they are kept in one of the higher humidity boxes for months. On the surface of the sample a soft, irregular material forms that does not have the same thickness everywhere. This material is much rougher than the surfaces in Figure 10. Also, the indents in this surface would go much deeper than those on a polished surface. The indents on the rough surface had a maximum depth of approximately 250 µm, while for the polished surfaces a maximum depth of 120 µm was rarely encountered. In addition to this, samples would also become larger in the high humidity boxes. As mentioned in Section 3.2, a polishing device was used to polish the samples until they were flush with the edges of the polishing device. This way they all have the same thickness and roughness. However, when samples were inserted into the device again after spending a long time in the high-humidity boxes, they were above the edges of the device again. Because of the size increase and the rough material on the surface, samples were polished again right before testing.

Before testing, the controlled humidity device was started so that the desired humidity in the climate-controlled chamber was reached before placing the sample in it. The settings of the Wetsys for the four middle humidity levels were a flow rate of 200 ml/min, an internal temperature of 22,4 °C and an internal relative humidity corresponding with the values in column 5 of Table 4. For the lowest saturation level, an external relative humidity of 12.5% was reached by using a flow rate of 200 ml/min, an internal temperature of 22.4 °C and an internal relative humidity of 8.4%. Finally, for the highest saturation level, a flow rate of 200 ml/min, an internal temperature of 80 °C and an internal relative humidity of 95% were used which lead to a maximum external relative humidity of 98%. The temperature in the climate-controlled chamber was not affected by the high internal temperature of the Wetsys. After the desired humidity was reached in the climate-controlled chamber, the sample to be tested was taken from the box, quickly polished again using the polishing device (Figure 8) and sandpaper, weighed, and placed into the climate-controlled chamber with the metal grid screwed on top of it. The samples were weighed again after testing to determine whether the weight had changed during the testing. After placing the sample in the chamber, the humidity in the chamber went down. Therefore some time was taken between the placement of the sample and the first test, so that the humidity could go back to the desired value.

4.1.3 Test routine

In order to perform multiple tests on one sample, the indenter stayed in its place while the cross tables were moved so that the sample was in a different location with respect to the indenter for each test. The indenter has a diameter of 8 mm. This means that using the cover with the 25 mm square hole, 17 mm is left for moving the indenter tip around above the sample. With the predetermined distance of 2 mm between two indents, 6x6 = 36 tests were done on one surface. Because of the hole in the cover, humid air can escape. For the lower humidity tests the flow rate of 200 ml/min was high enough to keep the humidity at the desired level. However, for the highest humidity, the maximum achieved humidity was 87%. For this reason another cover with a round hole with a diameter of 15 mm was used. Using this hole, only 3x3 = 9 tests could be done on one surface, so more samples were needed for the samples tested at the highest saturation level.

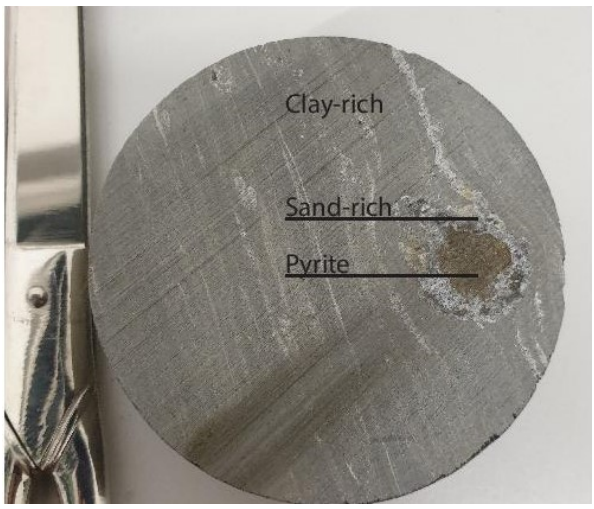

(a) *Slab that was used for cutting samples from. Bedding is clearly visible. A cluster of pyrite grains is surrounded by sand grains.*

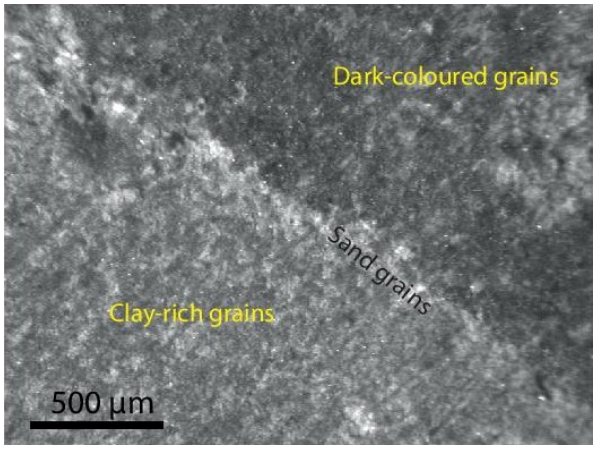

(b) *Microscope picture of a part similar to the cluster in figure 11a*

.

Figure 11

Before the start of the test the foot of the indenter goes down with a velocity of 2 mm/s until the sample is reached. When the foot touches the sample, the indenter, which is located 150 µm above the base of the foot, descends at a rate of 100 µm/s until it reaches the sample. The indentations were made controlled by force at a rate of 1.5 N/s. Then the maximum force of 15 N is held for one second. This is to minimize the effects of creep on the results. The reason a value of zero seconds was not chosen is that a holding period of zero seconds would give larger differences in the maximum force eventually reached. This is probably caused by the indenter tip having to go back up quickly. After the holding period of one second, the indenter tip goes up again at the same rate it went down (1.5 N/s). Before every test the microscope was used to analyse whether the part of the sample under the indenter was the grey clay or a cluster of other grains, because sand and pyrite grains give much higher hardness values than the grey clay parts. This is especially important in the sandy facies. Figure 11a shows a slab of sandy facies material that contains a cluster of pyrite with a rim of sand-sized grains around it. Looking under the microscope, a similar situation looks like Figure 11b. The part that is named "dark-coloured grains" in this part could be pyrite where the the distinct colour can not be seen due to the poor light conditions under the microscope and the fact that the camera is black-white. However, it could also be a feldspar rich part. These parts will be mentioned as dark-coloured grains. The light grains are larger than the shale grains and are assumed to be quartz, due to its features under the microscope combined with the fact that the sandy facies contains 22-44 wt% quartz (Table 2). The pyrite and quartz grains were avoided under the microscope because of their divergent hardness compared to the shale grains.

4.2 Water content

A random selection of two shaly facies and two sandy facies samples were saturated to 99,9% in the climate-controlled box. They were then taken out of the box, weighed and then dried in a Memmert heating and drying oven at 105°C. In the following days they were weighed daily until the weight remained equal for 2 subsequent days. The final weight subtracted from the initial weight is the water weight at 100%, assuming that all water evaporated. This value was divided by the initial weight to calculate the relative water content. The average values of the two shaly facies and the two sandy facies was taken to create a value of water content for both facies. This

value was used to calculate the relative change in weight while the samples were being tested to confirm whether the samples remained at their desired saturation level. This was done by multiplying the water content value with the initial weight to give the initial water weight and subtracting the initial weight before the test from the final weight from after the test to give the change in water weight. The change in water weight was then divided by the initial water weight and multiplied with 100 to give the percentage of saturation change.

4.3 Data analysis

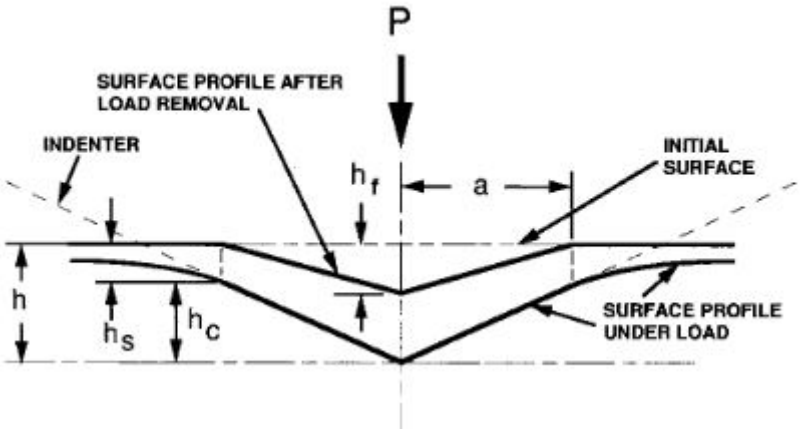

Figure 12: *A schematic representation of a section through an indent showing various quantities used in the analysis (Oliver and Pharr, 1992)*

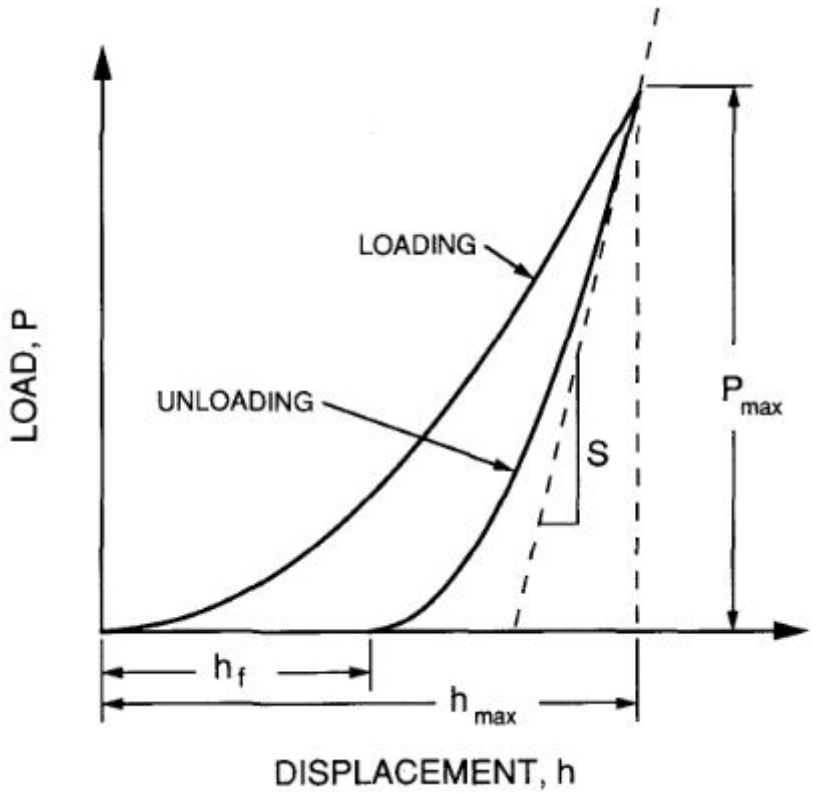

Figure 13: *A schematic representation of load versus indenter displacement showing quantities used in the analysis as well as a graphical interpretation of the contact depth. (Oliver and Pharr, 1992)*

The tests create an indent that looks like the one in Figure 12. This is the side view of an indent. Two situations are indicated: the bottom one is the surface profile under the maximum load. The upper profile is the surface profile after the load has been removed. The loading and unloading of the sample and the change in displacement are monitored by the indentation device and creates a graph that looks like that in Figure 13. The dashed line is a tangent line based on the initial slope of
unloading. The slope S is calculated from dP/dH and is the stiffness of the material. The hardness (H) of the sample can then be calculated using Equation 1. This gives the Vickers hardness number, which is calculated by the Zwick testXpert software.

For the Young's modulus modulus, first the projected area of the indent needs to be calculated. The area is calculated by

$$A_p = 24.5h_c^2 \tag{3}$$

As visible in Figure 12, h_c can be be calculated by subtracting the final depth of the indent h_s from the depth of the indent at the highest maximum force h. However, a geometry correction factor needs to be applied to the following equation from Fischer-Cripps and Nicholson (2004)

$$h_c = h - \epsilon(h - h_r) \tag{4}$$

where ϵ is the geometry correction factor for a Vickers indenter (0.75) and h_r is the displacement value found when the initial unloading slope S is extrapolated to the point where the load is zero crosses the x-axis (Figure 13).
h_c and S are then used to calculate the reduced elastic modulus (E_r), which represents the elastic deformation in plane strain condition that occurs in both sample and indenter tip. (Oliver and Pharr, 1992):

$$E_r = \frac{\sqrt{\pi}}{2}\frac{S}{\sqrt{A_c}} \tag{5}$$

The reduced modulus can the be used to calculate the indentation modulus with (Oliver and Pharr, 1992)

$$\frac{1}{E_r} = \frac{(1-v^2)}{E_{IT}} + \frac{(1-v_i^2)}{E_i} \tag{6}$$

which is then converted in order to be able to calculate the indentation modulus

$$E_{IT} = \frac{1-(v_s)^2}{\frac{1}{E_r} - \frac{1-(v_i)^2}{E_i}} \tag{7}$$

where (E_{IT}) and (v_s) are the indentation modulus and Poisson's ratio for the sample and (E_i) and (v_i) are the same parameters for the indenter. The indentation modulus is exactly the same as the Young's modulus or the elastic modulus. According to Oliver and Pharr (1992), the modulus E_i of the diamond indenter is 1141 GPa and the poisson's ratio v_i is 0.07. For Poisson's ratio of the sample, the best estimate values from Table 1 were used. As mentioned, the reduced modulus is the modulus in plane strain condition. That means that in this case where there is very little to no effect on the indenter (because the diamond indenter is so much harder than the rock), the indentation modulus will per definition be lower than the reduced modulus unless the Poisson's ratio is smaller than zero, which rarely happens, and does not happen here either. The Matlab code for calculation of the modulus of the sandy facies perpendicular to bedding is in Appendix A.

5 Results

5.1 Saturation change

Four samples were oven dried to assess the water content as described in Section 4.2. The average water content of the shaly facies is 0.067 while the average water content of the sandy facies is 0.054. These values were used to calculate the change in saturation based on the change in weight during the tests. The change percentages were divided into clusters of approximately equal values and plotted in the bar chart in Figure 14. The clusters were made so that the value -1 contains all values between 0 and -1, the value -2 contains all values between -1 and -2, etc. The value 0 means that there was no change in saturation during the test. The value 3+ contains one value of 11.017.

5.2 Hardness

Figure 15 contains four boxplots of saturation level plotted against modified Vickers hardness. The median is in the part of the box where there is a red line and a notch. The bottom edge of the box indicates the 25th percentile and the upper edge of the box indicates the 75th percentile. The whiskers extend to the most extreme data points not considered outliers and the 'plus' symbols imply outliers. A quadratic fit through the median values has been plotted as a red line and the equations of the quadratic fits are in the captions. The R^2-values are also plotted in the boxplots. The amount of tests for each point is in the figure as the value 'N'. All combinations indicate a decrease in hardness with an increasing saturation level. The quadratic fits show that the decrease in hardness is most distinct at higher saturation levels. Between 60% and 99% the slope is steeper than between 13% and 60%. This is especially true for the shaly facies. The absolute values inside the boxes are between 5 and 30 kg/mm^2 for the sandy facies and between 3 and 20 kg/mm^2 for the shaly facies. For all four combinations of direction to bedding and facies, the quadratic fits fit inside the boxes, except for the 45% saturation in figure 15c. Significant outliers can be seen in especially the sandy facies. The outliers are mostly above the boxplots. Many of the outliers have a hardness value of 1.5 - 2 times the median value. The shaly facies contains much fewer outliers, and the outliers that exist are much closer to the median than in the sandy facies.

Figure 16 contains the four quadratic fits of the median values of the hardness. The diamonds are the medians corresponding with the colour of the quadratic fit lines. The sandy facies values have a consistently higher hardness value than those from the shaly facies. For the sandy facies, the median value of the parallel tests is equal to the perpendicular tests at 13% saturation.

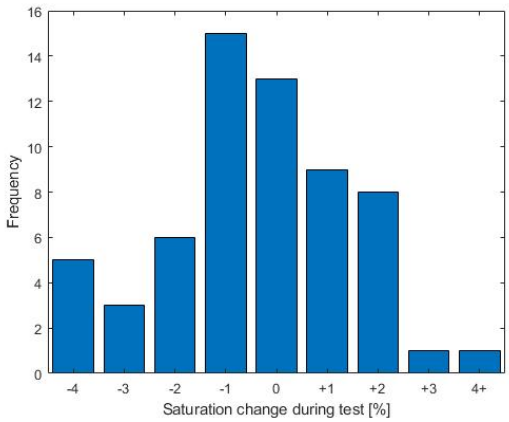

Figure 14: *Bar chart of saturation change in the climate-controlled chamber during tests.*

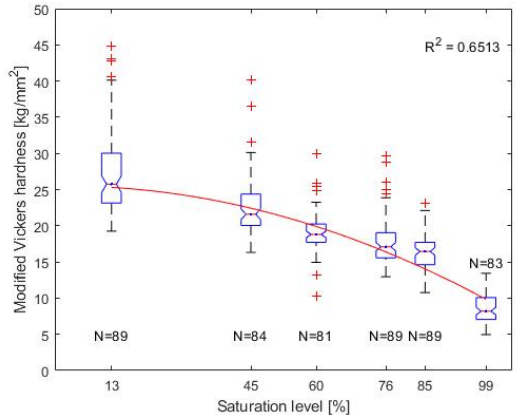

(a) *Sandy facies Perpendicular.*
Quadratic fit: $f(x) = -0.001665x^2 + 0.006603x + 25.5$

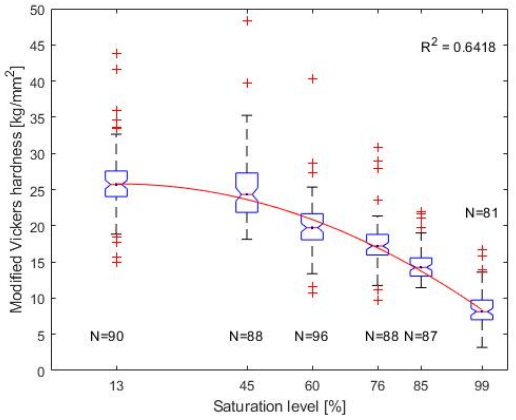

(b) *Sandy facies Parallel.*
Quadratic fit: $f(x) = -0.002508x^2 + 0.07879x + 25.16$

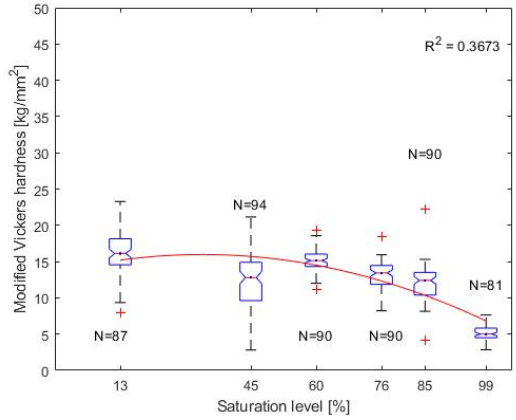

(c) *Shaly facies Perpendicular.*
Quadratic fit: $f(x) = -0.00216x^2 + 0.1465x + 13.49$

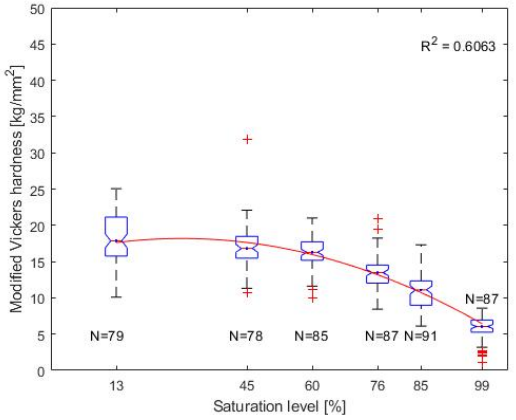

(d) *Shaly facies Parallel.*
Quadratic fit: $f(x) = -0.002472x^2 + 0.1486x + 15.59$

Figure 15: *Boxplot of saturation level vs. Modified Vickers hardness for different combinations of facies and direction with respect to bedding. N-values are plotted in the figures. The red lines are a quadratic fit of the medians of the different saturation levels. Quadratic fit equations are in the subcaptions.*

Table 5: *Vickers hardness values at saturations of 13% and 99%. Difference in ratio between saturations and between facies for the same direction P stands for parallel and N for normal/perpendicular.*

Hardness	13% [kg/mm^2]	99% [kg/mm^2]	Ratio
Sandy P	25.7	8.1	3.17
Sandy N	25.7	8.2	3.13
Shaly P	17.9	6.0	2.98
Shaly N	16.1	5.0	3.22
Difference sandy P - shaly P	7.80	2.10	
Ratio sandy P - shaly P	1.44	1.35	
Difference sandy N - shaly N	9.60	3.20	
Ratio sandy N - shaly N	1.60	1.64	

In the centre of the diagram, the parallel values are higher. Then, at the 76% point they are equal again, and for the highest saturations the perpendicular tests have a higher hardness than the parallel tests. For the shaly facies the parallel values are consistently higher than the perpendicular values, except for at the 76% mark, where they are equal, and the 85% mark, where the perpendicular value is higher than the parallel value. The hardness decreases with increasing saturation. The ratio between the hardness at 13% saturation and 99% is between

2.98 and 3.22 for all data sets (Table 5). The difference between the sandy and shaly facies decreases with increasing saturation as well. The ratio between sandy P and shaly P decreases with 0.09 and the ratio between sandy N and shaly N increases with 0.04 between the saturations of 13% and 99%. So the hardness values decrease, but the ratios between the different data sets remain similar. The R^2-values are also plotted in Figure 15. The values for the sandy facies and the shaly facies parallel data sets are all between 0.6 and 0.65. The shaly p value is 0.37, so the fit of the shaly parallel is not as good as the other values.

As mentioned in Section 4.1.3, the microscope was used in order to estimate whether the surface in the test location was the regular mix of minerals in the light grey part of the rock, and not a lens or cluster of sand, pyrite or feldspar rich material. However, sometimes a test was already performed when it was noticed that there was a quartz or dark-coloured cluster below the indenter. These values have been plotted in Figure 17. These are two subsets of tests that are not included in the other sets plotted in Figures 15 and 18. The amount of tests per saturation level varies highly because the samples were cut and divided randomly between the climate-controlled boxes. Therefore whether there were clusters of quartz or pyrite material was controlled by chance and many saturation levels are not incorporated in these figures because there was no or not enough data. All these values are from sandy facies samples, because no clusters of different material were found in the shaly facies. The dark-coloured grains perpendicular shows that hardness values were found from 30 of up to 350 kg/mm^2. For the quartz grains parallel values differ between 10 and 180 kg/mm^2. For the quartz grains parallel, hardness values are between 25 and 190 kg/mm^2. These values are much higher than those at for the subsets of the regular tests. The scatter of all three combinations of grain type and orientation have a larger spread than the boxplots in Figure 15. There is also a trend of hardness downwards with increasing saturation levels. Figure 17d contains the linear and quadratic fits of the median values. There is a clear downward trend. The hardness values are much more similar at higher saturation level than at lower saturation level.

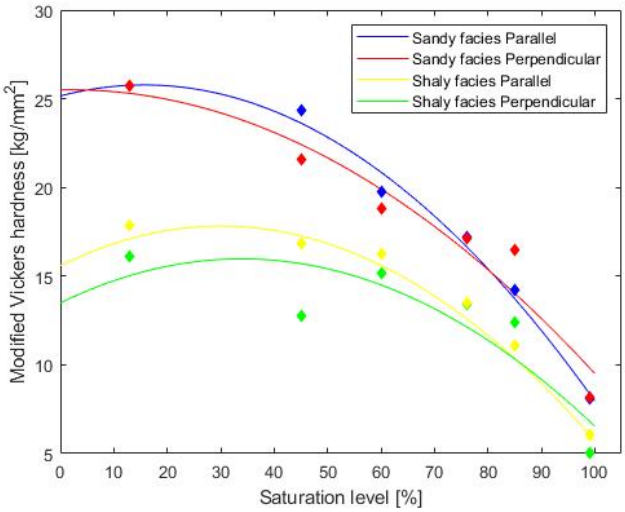

Figure 16: *All combinations of testing direction and facies together. The points are the median Vickers hardness values at different saturations. The lines are the quadratic fits of the median hardness values as in the subcaptions of Figure 15. Note that the box and whiskers in Figure 15 are needed to see whether there is overlap between the points.*

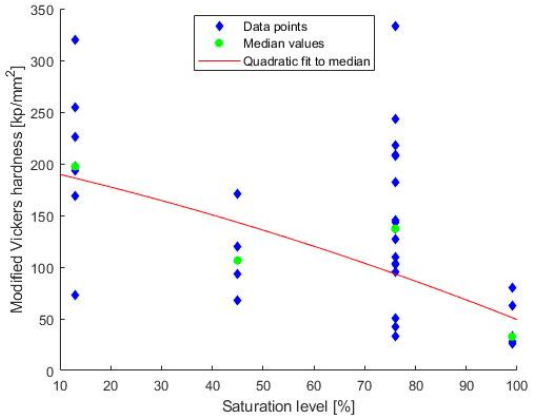

(a) *Scatter plot of dark-coloured grains perpendicular. Quadratic fit:* $f(x) = -0.004262x^2 + -1.092x + 201$

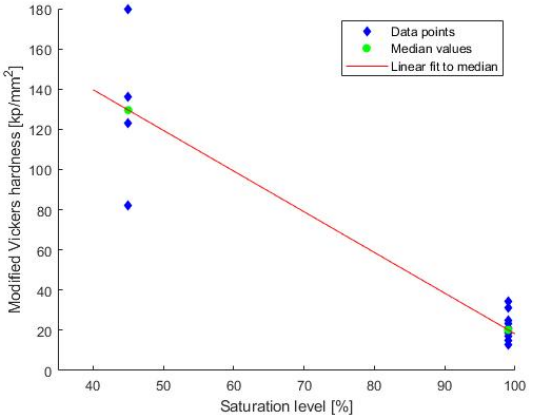

(b) *Scatter plot of quartz grains perpendicular. Linear fit:* $f(x) = -2.025x + 220.7$

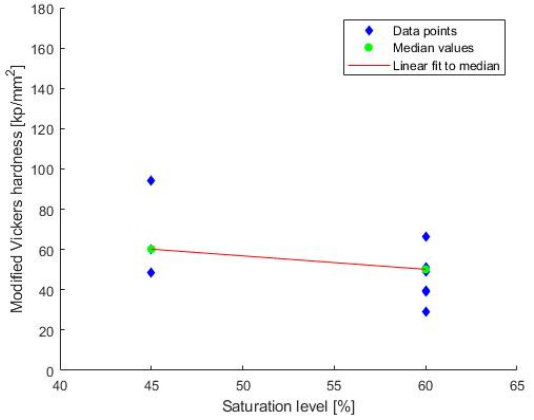

(c) *Scatter plot of quartz parallel. Linear fit:* $f(x) = -0.6668x + 90.17$

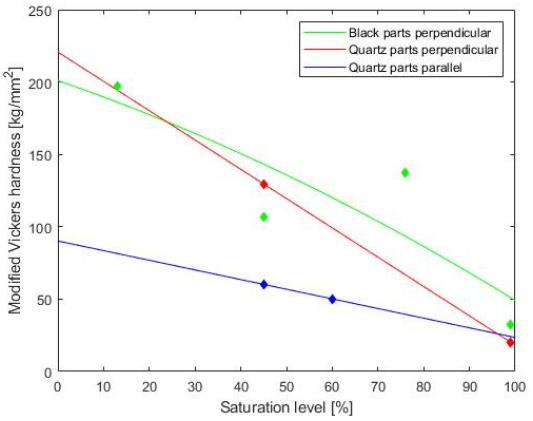

(d) *Medians of dark-coloured and quartz grains together.*

Figure 17: *Scatter plot of saturation level vs. Modified Vickers hardness for different grain subsets and direction with respect to bedding. N-values are plotted in the figures. The red lines are a quadratic or linear fit of the medians of the different saturation levels. Fit equations are in the subcaptions.*

5.3 Modulus

Figure 18 shows the reduced modulus and the indentation modulus for all different combinations of facies and test orientation with respect to bedding. For the calculation of the indentation modulus, the best estimate of Poisson's ratio from Table 2 was used. However, these best estimate values are based on the range that has been found. These ranges are very wide in some cases, and also exhibit substantial overlap. The reduced modulus should be considered when looking at the relationship between the different saturation levels, facies and test direction because the relationship is not affected by the difference in Poisson's ratio. The ratio between the reduced modulus and the indentation modulus differs between the different series of direction to bedding and facies, but is very similar within within a series for different saturation levels. The average ratios of reduced modulus to indentation modulus for shaly perpendicular, shaly parallel, sandy perpendicular and sandy parallel are 1.12, 1.05, 1.05 and 1.22, respectively. The indentation modulus values are more true to the actual elastic modulus values of the rock because the effect of the deformation of the indenter has been accounted for. The meaning of the boxes and bars is the same as described for Figure 15, just as the N-values and the quadratic fit lines. The quadratic fit equations are in the subcaptions. For the reduced modulus, the spread in values is smaller than for the HVT values. The boxes and whiskers are smaller, and there are fewer outliers that are also located closer to the boxes. For all data sets the reduced and indentation

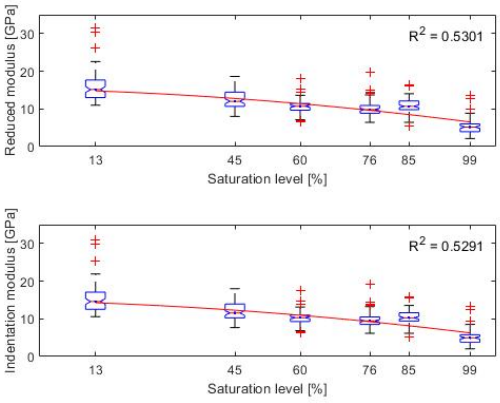

(a) *Sandy facies Perpendicular.*
Quadratic fit E_r*:* $f(x) = -0.0006177x.^2 - 0.0283x + 15.46$
Quadratic fit E_{it}*:* $f(x) = -0.0005866x^2 - 0.02883x + 14.93$

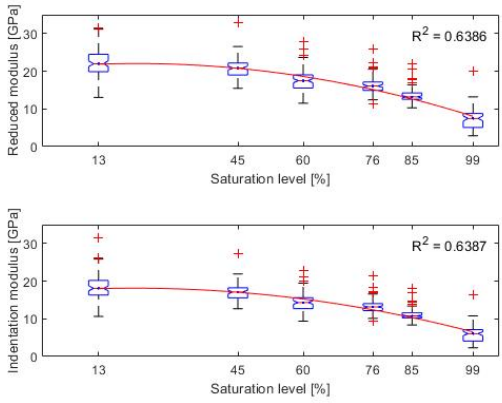

(b) *Sandy facies Parallel.*
Quadratic fit E_r*:*$f(x) = -0.002346x^2 + 0.1018x + 20.95$
Quadratic fit E_{it}*:* $f(x) = -0.001926x^2 + 0.08238 + 17.25$

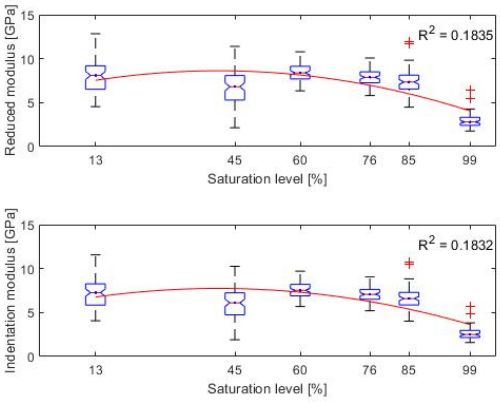

(c) *Shaly facies Perpendicular.*
Quadratic fit E_r*:* $f(x) = -0.001369x^2 + 0.1129x + 6.301$
Quadratic fit E_{it}*:* $f(x) = -0.001231x^2 + 0.1014x + 5.651$

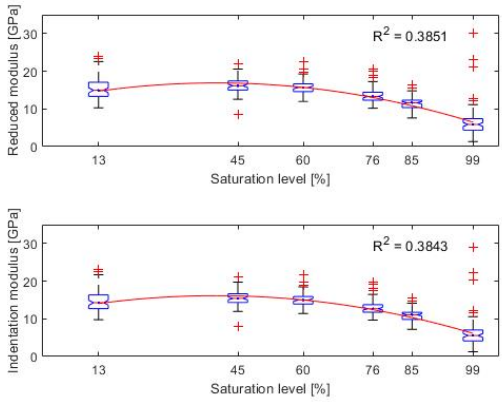

(d) *Shaly facies Parallel.*
Quadratic fit E_r*:* $f(x) = -0.002997x^2 + 0.2399x + 12.1$
Quadratic fit E_{it}*:* $f(x) = -0.002879x^2 + 0.2304x + 11.54$

Figure 18: *Boxplot of saturation level vs. reduced modulus and indentation modulus N-values are equal to those in Figure 15. The red lines are a quadratic fit of the medians of the different saturation levels. Quadratic fit equations of both moduli are in the subcaptions. Note that the scale is different for Figure 18c*

.

moduli decrease with increasing saturation. For the sandy facies perpendicular values, the quadratic fit is almost linear, while for the other three, the quadratic fit shows a moderately sloping to flat slope for the lower saturation levels, while the slope steepens downwards towards higher saturation levels. For the shaly facies values, the median of the 13% saturation values is lower than the 60% saturation median. Because of this, in the quadratic fit line there is an increase in modulus between 15% and 45%. When not looking at the quadratic fits, it stands out that a lot of the decrease in reduced modulus is made between 85% and 99%, while between 13% and 60% the values are almost equal to each other. This is especially in the perpendicular tests. in the shaly facies perpendicular values, the reduced modulus value changes from 8.1 to 7.3 GPa between 13 and 85%, and then jumps from 7.3 to 2.8 GPa in the last step to 99%. This is the most extreme example, but this phenomenon of a larger decrease in the higher saturation levels is present. The reduced modulus values are all between 3 and 20 GPa for the sandy perpendicular tests and between 3 and 10 for the shaly perpendicular tests, outliers excluded. The reduced modulus for the parallel tests are all between 5 and 25 GPa, outliers excluded. R^2 is plotted in Figure 18 as well. The difference in fit between the reduced modulus and indentation modulus differs by 0.01 at the most. Like in the hardness values, the R^2 values of the shaly

facies are lower than those of the sandy facies. For the modulus, the R^2 values of the parallel tests are also higher than those of the perpendicular tests.

Figure 19 shows the quadratic fits of the modulus median values. As mentioned, for this figure the reduced modulus graph is the most accurate. It is clear that here the direction to bedding is more dominant than the type of facies, as the two lines from the parallel tests and the two lines of the perpendicular tests are paired together. The tests parallel to bedding have a higher reduced and indentation modulus than the tests perpendicular to bedding. Furthermore, the sandy facies samples have a higher reduced and indentation modulus than the shaly facies samples. The medians of the subsets stay in the same order for all saturation levels, except for the shaly facies parallel, which is almost equal to sandy facies perpendicular at 13, 85 and 99%. For all combinations of direction and facies, the ratio between the median of reduced modulus at 13% and at 100% is between 2.5 and 3.0 (Table 6). Just like with the hardness data, the difference between the higher values and the lower values is much larger at the lower saturations than at the higher saturations. In the case of the modulus, this concerns the difference between the parallel and perpendicular values of one facies. As visible in Table 6, the ratio between sandy parallel and sandy perpendicular changes from 1.43 to 1.44 while the ratio of shaly parallel to shaly perpendicular changes from 1.84 to 2.07. So here, the reduced modulus decreases with a ratio of between 2.5 and 3.0, while the ratio between the different tests barely changes.

Table 6: *Reduced modulus values at saturation levels of 13% and 99%. Differences and ratios between the different directions for the same facies. P stands for parallel and N for normal/perpendicular.*

Reduced modulus	13% [GPa]	100% [GPa]	Ratio
Sandy P	22	7.5	2.93
Shaly P	14.9	5.8	2.57
Sandy N	15.4	5.2	2.96
Shaly N	8.1	2.8	2.89
Difference sandy P - sandy N	6.6	2.3	
Ratio sandy P - sandy N	1.43	1.44	
Difference shaly P - shaly N	6.8	3	
Ratio shaly P - shaly N	1.84	2.07	

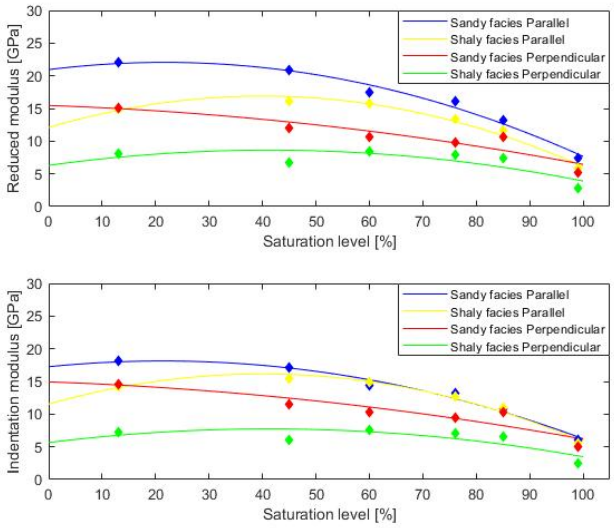

Figure 19: *All combinations of testing direction and facies together. The points are the median reduced and indentation moduli at different saturations. The lines are the quadratic fits of the median modulus vales as in the subcaptions of Figure 18. Note that the box and whiskers plots in Figure 15 are needed to see whether there is overlap between the points.*

6 Discussion

6.1 Sample preparation and experiments

In Section 4.1.2, it was mentioned that samples kept in the high-humidity climate-controlled boxes acquired an irregular, rough and very soft material on the surface. In addition to this, the material expanded, which was noticed by the fact that the surface was higher than immediately after polishing. The increase in surface height was oberserved to be up to 0.5 mm. The observed material could be gypsum. Bossart et al. (2004) found gypsum spots in OPA in Mont Terri in the first 50 - 100 cm from the tunnel wall where frequencies of up to 35 fractures/m were observed. These zones were interpreted as zones with fractures that are filled with air where oxidation reactions might have occurred. This gypsum is formed when an oxidation halo made up of interconnected fractures around the tunnel is formed. The gypsum was found on fracture surfaces and was formed from the oxidation of pyrite and precipitation due to evaporation of the pore water. Gypsum crystals were only found in these shallow parts of the EDZ, where an interconnected fracture network exists. A second option is that the observed surface changes are created by swelling of clay minerals. The clay minerals would expand everywhere in the sample, so also on the surface, and create an irregular sample surface. This would also explain the increase in surface height with respect to the polishing device.
The data from the bar chart in Figure 14 contains data of 61 out of approximately 100 tests done. The data suggests that deviations from the desired test saturation of more than 4% are very rare. 51 Out of 61 (83.6%) tests are within 2 percent from the desired saturation. 60 out of 61 tests (98.4%) are within 4% of the desired saturation. From this data, it can be stated that the samples were tested at the desired saturations, and that the deviations are insignificant.

6.2 Hardness

6.2.1 Statistical analysis

The plot of the quartz and dark-coloured grains (Figure 17) show a very wide range of hardness values that go up to 350 kg/mm^2. As mentioned, this because these tests were done in parts of

the sample surfaces that looked different (different colour and grain size) and contained a higher proportion of quartz, pyrite and feldspar. The high spread in the values can be explained by a difference in the proportion of these harder minerals. A cluster with 80% quartz and 20% clay minerals will be softer than a cluster with 90% quartz and 10% clay minerals, while they both look the same on the surface, so are in the same subset. In Figure 15, most of the outliers are above the whiskers of the boxplots and not below, and they are also mainly in the sandy facies. Based on figure 17, it can be said that these high outliers are parts of the samples were there is a higher proportion of quartz, pyrite and feldspar. For the outliers below the whiskers of the boxplot, it is possible that these are caused by large pores located in the location of the indentation test. When there are large pores, the indenter goes down with more ease which creates a lower hardness at this location. It is assumed that these outliers do not have a significant effect on the results. The median is used in order to exclude extreme values.

The R^2-values are higher for the sandy facies for both the hardness and the modulus values. This might be caused by the fact that the shaly facies samples were located in the climate-controlled boxes for much longer. The shaly facies samples were cut and ready to be tested, when an unexpected event delayed testing by months. Because of this, the shaly facies samples were in the climate-controlled boxes for 4 - 5 months. The sandy facies samples were in the boxes for approximately one month. this means that for the shaly facies there was much more time for dessication cracks to form in the lower humidity boxes and for the surface to get affected by the higher humidities (swelling and crystal formation). This can also be an additional cause of the large whiskers and the outliers for the hardness boxplots Another possible reason for the low R^2 values is that the quadratic fit does not work very well for this data. This can be attributed to the big jump in hardness between 85% and 99% saturation, while the rest of the graph is a lot flatter. This is mainly seen in the shaly facies tests. This is not captured in the quadratic fit, which can explain why the R^2 values are lower for the shaly facies.

6.2.2 The effect of mineralogy and anisotropy on hardness

The sandy facies hardness is approximately a factor 3 higher than that of the shaly facies. This can be attributed to the fact that the sandy facies contains a much higher percentage of quartz (Table 2). Also, the parallel values are higher than the perpendicular values when looking at Figure 16. This is counter-intuitive, because it is expected that it is easier to create an indent when the indenter pushes between the layers, compared to when it pushes perpendicular to the layers. It is constantly higher, and this can be explained by the closure of microcracks which creates more strain in the perpendicular direction. These microcracks were formed during desaturation and resaturation. This is further explained in Section 6.3.3. However, when looking at the boxes in Figure 15, they extend further than the difference between the values of parallel and perpendicular. For example, the median hardness value at 13% of shaly parallel is 17.9 kg/mm^2 and for shaly perpendicular it is 16.1 kg/mm^2. The boxes of the 13% values of shaly facies parallel and shaly facies perpendicular extend from approximately 17 to 22 kg/mm^2 and from 15 to 19 kg/mm^2, respectively. Therefore it can not be said with certainty that the parallel samples have a higher hardness than the perpendicular values.

6.2.3 The effect of saturation on hardness

The hardness decreases with increasing saturation. There is a a steep slope between 60% and 99% saturation while the hardness between 15% and 60% is almost constant. Especially for the shaly facies perpendicular a large part of the decrease in hardness is in the final 14% of the saturation increase. Michalopoulos and Triandafilidis (1976) researched change in indentation hardness and unconfined compressive strength for different rock types, of which the one closest to a claystone is a sandstone. A decrease in hardness and unconfined compressive strength with

increasing saturation was also found here. Here it was attributed to the softening effect that pore water has on the bonding strength of the rock. Azhar et al. (2020) performed micro-indentation, XRD, SEM and microscopic analysis in order to measure the effects of saturation on clay-rich sandstones. Two sandstones were tested of which the zone A sandstone contains 20.6% clay minerals and the zone B sandstone contains 11.4% clay minerals. In both of them, the clay minerals are mica/illite, kaolinite and montmorillonite. The other minerals present are quartz, feldspar and calcite. The zone A sandstone has an elastic modulus of 11 GPa unsaturated, and the zone B sandstone an elastic modulus of 17 GPa unsaturated. That is quite similar to the values of the indentation modulus for the sandy facies at 13% saturation.

For these tests, samples were not placed in a high humidity environment but submerged in water. Then, properties like elastic modulus and indentation hardness were tested according to the time they had spent in water. They found a decrease in hardness with increasing saturation of 89% and 99% for the zone A and B sandstones, respectively. That means that the effect of saturation on hardness is higher for the rock with a lower clay content. This is the other way around in this research, which is apparent in Table 5. The ratios between 13% and 99% saturation are higher for shaly facies, indicating that in the shaly facies there is a higher dependency on saturation. The hardness decrease is attributed to 1) the vanishing of temporary depositional bonds 2) weakening of diagenenetic bonds by dissolution and 3) a pressure increase on the framework of grains created by the swelling nature of the montmorillonite that causes damage to the rocks. The weakening of diagenetic bonds by dissolution does not occur in these experiments, because fysical water is needed for dissolution to occur. Also, there is no montmorillonite in OPA, so this does not have an effect on the rock. The bentonite backfill material does contain a large amount of montmorillonite, so this could affect the backfill material. However, the illite/smectite layers also swell in high saturation environments. Therefore, damaging of the rock by swelling is expected to be an important cause of the softening with increasing saturation. The clay percentage is higher in the shaly facies. Therefore, Swelling being the most important process in decreasing hardness also explains why the decrease in hardness is larger for the shaly facies. Finally, the ratio between the sandy and shaly facies values barely changes, which means that the effect of facies on the hardness does not change with saturation. So it can be interpreted that change in saturation does not affect the effect of grain type and anisotropy on hardness.

6.3 Modulus

6.3.1 Statistical analysis

There are fewer outliers for the modulus data and they are also relatively closer to the boxes compared to the hardness data. There are more outliers for the sandy facies than for the shaly facies. Also for the modulus data, the outliers that exist are mainly located above the boxes. This can as well be explained with the different amounts of feldspar, quartz and pyrite in the rock. These minerals are stiffer and thus a test in a cluster of these minerals will give a higher modulus compared to a part of the sample surface with an average amount of all minerals as in Table 2. The R^2 values of the reduced and indentation modulus are almost identical for the different combinations of test direction and facies. Also here, the R^2 is lower for the shaly facies tests than for the sandy facies. This could again be attributed to the fact that especially in the shaly facies tests there is a large jump in modulus between 85% and 99% and a more constant trend between 15% and 85%. Also for the modulus, this happens mainly in the shaly facies. Another reason for the lower R^2 values in the shaly facies could be the fact that the shaly facies samples were in the climate-controlled boxes for a longer amount of time, as is explained in section 6.2. The observed microscale modulus values are much higher than the macroscale values in Table 1, especially for the lower saturation levels. This is due to irregularities on the microscale, like pores and pre-existing cracks (Keller et al., 2017).

6.3.2 The effect of saturation on the modulus

The modulus decreases with increasing saturation, with most of the decrease between 75% and 99% for the parallel tests and between 85% and 99% for the perpendicular values. For the rest of the graph the values are almost constant or there is a small decrease of modulus with increasing saturation level. As mentioned Sn section 1.5, Wild et al. (2015) used the same method to saturate Opalinus Clay in order to perform various tests on it. Young's modulus was found using unconfined compression tests and obtaining the Young's modulus from the linear part of the stress-axial strain curve at low axial stresses. The saturation was connected to the suction. The total suction (referred to as suction from here) is the sum of capillary and osmotic suction. Capillary suction consists of capillary forces that arise from the pressure difference between the non-wetting and the wetting fluid at the gas/liquid boundary. Osmotic suction is created by osmotic processes. These process are consistently seen as a cause of increasing stiffness and strength with decreasing moisture content. A compressive contact pressure between grains is caused by surface tension at the boundary between air and water in adjoining voids. This is not a cohesive strength component, but it does have the same effect as if the grains were held together. This is why it is often called the apparent cohesive strength component (Peterson, 1988). Experimental data was fitted to the Van Genuchten equation (Van Genuchten, 1980) to

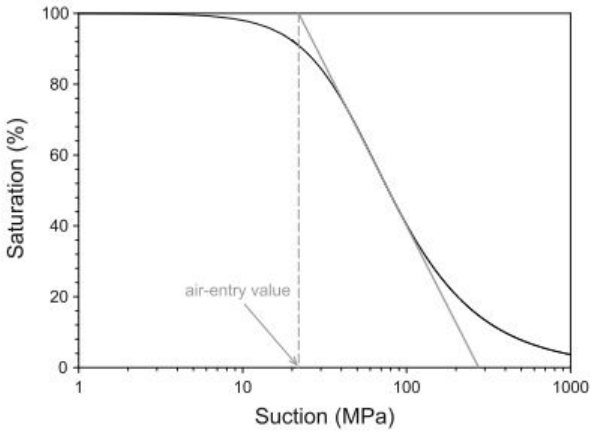

Figure 20: *Relation between suction and saturation. The lighter straight line is the Van Genuchten fit (Wild et al., 2015)*

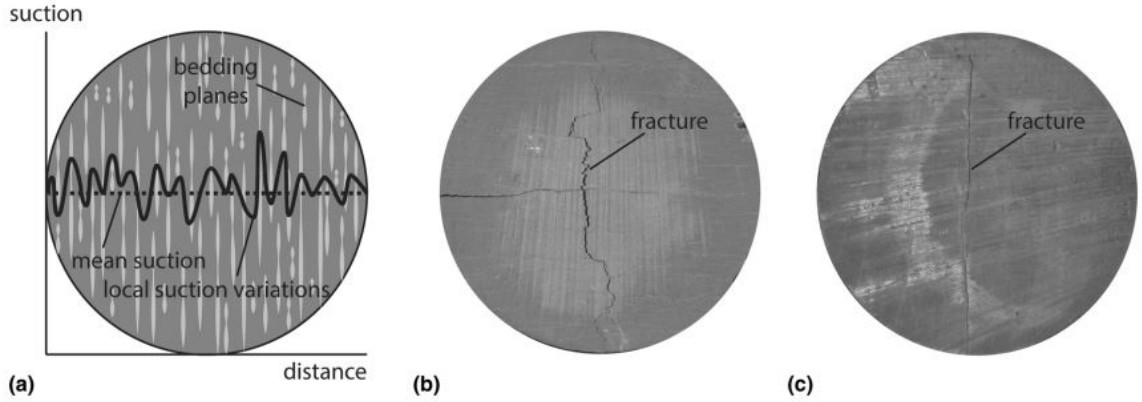

Figure 21: *a) Local suction varieties in the different bedding planes. b) A fracture in a sample loaded perpendicular to bedding migrates to the locations with the highest suction. c) A fracture in a sample loaded parallel to bedding follows the bedding (Wild et al., 2015)*

create Figure 20. This figure shows the relation between suction and saturation. The suction is

0 MPa at a saturation of 100% saturation and 1000 MPa at 5% saturation. They are inversely correlated because a decrease in water increases osmotic and capillary suction. When the rock is fully saturated there is no strength field between water and air, so there is also no suction. Wild et al. (2015) found that the Young's modulus increases linearly between a suction of 0 and 56.6 MPa and that from 56.6 to 224.9 MPa, the suction remains roughly equal. 56.6 MPa equals roughly 65% saturation, according to Figure 20. That means that the elastic modulus remains equal from 0% to 65% saturation and there is a steep, linear decrease in modulus between 65% and 100% saturation. This fits with the findings in this research, and the suction effect can explain the observed decrease in modulus with increasing saturation.

6.3.3 The effect of anisotropy on the modulus

Wild et al. (2015) tested parallel to bedding, which means these findings are consistent with the findings for the modulus in parallel direction. In Figures 18b and 18b it can be seen that both for the reduced and indentation modulus between 13% and 60%, the modulus is almost constant and does not change much, while between 60% and 99% there is a linear decrease. However, the findings are not consistent with the tests perpendicular to bedding. Here the constant part extends further, from 13% to 85% saturation and the decrease in modulus occurs between 85% and 99% saturation. This might be caused by a variation in pore distribution. Houben et al. (2013) found that most pores in the Opalinus Clay are aligned parallel to bedding. That means that when a load is applied parallel to bedding, cracks grow along bedding layers (Figure 21b). Wild et al. (2015) also found that the suction is not distributed uniformly throughout the sample due to the ununiform distribution of pore space (Figure 21a). What happens because of this is that when loaded perpendicularly, fractures will grow sub-parallel to bedding and arrest at high-suction layers with lower strength and stiffness (Figure21c). This means that for loading perpendicular to bedding, the suction needed to change the stiffness is very small because a small change in suction already creates a heterogeneity that can make the fracture grow. The fact that in this research the findings are similar as in Wild et al. (2015) means that it can be concluded that the effect of saturation on the modulus in Opalinus Clay is similar between the macro- and microscale.

(Zhang et al., 2012) performed micro-indentation tests on the Callo-Oxvordian shale (COX) and found that the elastic modulus is systematically higher for tests parallel to bedding compared to tests perpendicular to bedding. This is consistent with our findings. This is caused by the progressive closure of microcracks. Because cracks are formed parallel or subparallel to bedding, there is more strain caused by closure when loading is done perpendicular to bedding. This increase in strain causes a lower stiffness for the perpendicular tests. They also found that the elastic modulus in the perpendicular direction is less sensitive to saturation degree than in the parallel direction. For these tests the elastic modulus at 55% saturation is approximately 4 GPa parallel to bedding and 2 GPa for perpendicular to bedding. At 99% saturation the elastic modulus is approximately 1.4 GPa parallel to bedding and 1.2 GPa for perpendicular to bedding. That means that for the perpendicular tests, the modulus decreases by a factor 2.86, while for the parallel tests the decrease is with a factor 1.67. As visible in the ratio column of Table 6, in these results there is also a difference in the ratio between the parallel and perpendicular tests. However, this difference is not nearly as big as in the results of Zhang et al. (2012). Additionally, for the results in this research the effect of anisotropy on the effects of saturation is the other way around: the effect of saturation on the modulus is greater for the tests perpendicular to bedding for both the sandy and shaly facies. Because the differences are so small it can be concluded that for these experiments, anisotropy does not have an effect on the sensitivity of the elastic modulus to saturation and desaturation. According to Zhang et al. (2012), the fact that for COX shale the elastic modulus in the parallel direction is more sensitive to saturation degree than that in the perpendicular direction is caused by the structural effects of bedding

planes swelling with increasing saturation. The fact that that does not happen here, is possibly that the aforementioned effect of closure of microcracks is more important in the Opalinus Clay than in the COX clay. Another possibility is related to mineralogy. As in Table 2, the weight percentage of clay minerals in the Opalinus Clay vary strongly. In this research, as in the Zhang et al. (2012) research, no mineralogy measurements were done. However, it is possible that in the COX clay swelling has a greater effect on the elastic modulus because there are more smectite minerals in the COX clay. Further research could be performed to analyse the effect of mineralogy on the relation between anisotropy and saturation/suction.

6.4 Final remarks on the discussion

The fact that for the reduced modulus the sandy facies contains higher values than the shaly facies can again be attributed to the clay/quartz content. In turn, the fact that for the hardness the parallel values are generally higher can be attributed to the closure of microcracks. For the hardness values the shaly facies and sandy facies values are grouped together, while for the modulus values the parallel and perpendicular values are grouped together (Figures 16 and 19). This means that the hardness, which is the resistance to plastic deformation is mostly affected by the mineralogy. The elastic modulus, or stiffness, is the resistance to elastic deformation. This is mostly affected by anisotropy and the closure of microcracks. On the basis of the ratio columns in Tables 5 and 6, it can also be concluded that the effect of saturation on hardness is slightly greater than the effect on the modulus. In this discussion, a clear distinction is made where breaking of bonds and internal pressure on the framework of grains caused by swelling of clay minerals is seen as the main cause of decreasing hardness with increasing saturation and suction is seen as the main cause of decreasing stiffness with increasing saturation. This distinction can be made because the breaking of bonds is plastic deformation and therefore has an impact on the hardness while the results of suction are reversible processes and therefore have a larger effect on the stiffness. However, both these processes probably have a slight effect on both hardness and stiffness. Also, the causes for decrease in the values of these properties are based on literature and not on observations. Whether this is true could be tested by testing two different types of clay shale where one contains swelling clays like smectites and the other does not. For these experiments nothing can be said about this because as seen in Table 2, there is overlap between the sandy and shaly facies on the percentage of illite/smectite mixed layers.

6.4.1 Effects on self-sealing properties and recommendations

The fact that the sandy facies samples have both a higher modulus and a higher hardness mean that they are less likely to deform. This means that it could prove worthy to look into this facies for the storage of nuclear waste. However, the lower hardness for the shaly facies is caused by swelling, and indicates that there is more swelling with an increase in saturation level. Swelling is one of the self-sealing processes. So it is important to know whether it is favourable to store nuclear waste in a rock that is less easily deformed, or in a rock type that is more easily deformed, but has a better ability of self-sealing.
Because fractures in Opalinus Clay will almost always form parallel or subparallel to bedding, the fracture surface is always perpendicular or subperpendicular to bedding. The percentage of the increase in both hardness and decreased modulus with decreasing saturation between 99% to 85% is the highest for the shaly facies perpendicular (Table 7). Also for the parallel values it is much higher for the shaly facies as well. That means that in the open-drift stage of the repository formation, the hardness of the fracture surfaces will change much faster with decreasing and increasing humidity than those of the sandy facies. So with seasonal variations in humidity, the fracture surfaces of the shaly facies will increase and decrease in hardness and stiffness much faster than the sandy facies. That means that in a period of lower humidity, like the open drift stage, the shaly facies will be affected less by forces like increasing overburden

pressure than the sandy facies. On this basis it would be logical to advice on using the shaly facies for nuclear waste storage. On the other hand, the self-sealing processes of swelling, slaking and creep of the fracture wall material will decrease because of the increase in hardness and stiffness. Secondly, swelling also damages the rock, and the data suggests that the repetitive swelling and shrinking of clay minerals will have a greater effect on the shaly facies. However, when the nuclear waste has been stored and the tunnels closed, the saturation will increase and might allow these self-sealing processes to occur again. So on the long-term scale this will probably not have an effect on self-sealing processes. This means that the advice to use the shaly facies depends on whether the increase in stiffness and hardness with decreasing saturation is more important than the repetitive damage created by the swelling and shrinking of the clay minerals. More research should be done to analyse which of these is true.

Table 7: *Increase in hardness and reduced modulus between 99% and 85% as a part of the total increase. It is clear that for the shaly facies this is much higher for both perpendicular and parallel.*

Facies and direction	Hardness increase 99-85%	Reduced modulus increase 99-85%
Shaly perpendicular	66.6	85.9
Sandy perpendicular	47.0	55.2
Shaly parallel	42.8	63.4
Sandy Parallel	34.8	39.5

7 conclusions

Micro-indentation tests were performed on Opalinus Clay shale with a variation in test direction with respect to bedding, saturation level and facies (mineralogy). The goal was to require data for the hardness and modulus/stiffness and relate this to the three different mentioned variations. A climate-controlled chamber built around the test set-up bears enough effect on the desaturation of the samples that in 98% of samples tested there was a resaturation or desaturation of a maximum of 4% relative humidity. For both hardness and stiffness a decrease was found with an increase in saturation. Between 13% and 99% the hardness decreased by a factor 2.98 to 3.22. The reduced modulus decreased by a factor 2.57 to 2.96 for the same range of saturation levels. For the modulus, this is caused by a decrease in suction with increasing saturation. For the hardness, swelling of clay minerals breaks the bonds in the rock which makes it softer. However, both of these processes will have a slight effect on the other property as well. Further research should be done to analyse whether microcrack closure also has an effect on the hardness. This could be done by testing two different shales, of which one contains swelling clays and the other one does not. This effect had previously only been observed in clays for the modulus on the macroscale. It can now be concluded that the effect of suction also exists for the modulus on the microscale. Based on the ratio values there is a slightly larger effect of saturation level and suction on the hardness than on the modulus. Also for both stiffness and hardness the values are lower for perpendicular tests compared to the parallel tests. This is caused by sealing of microcracks formed during desaturation and resaturation. These microcracks are formed parallel or subparallel to bedding, which means they are closed when stress is exerted perpendicular to bedding. The resulted strain does not occur in the tests parallel to bedding which is why the modulus/stiffness is higher for the parallel tests. Finally, both modulus and hardness are higher for the sandy facies than for the shaly facies. This is caused by the higher quartz content in the sandy facies. For the hardness, the facies/mineralogy has the greatest impact, while for the modulus, the direction to bedding is the most important factor that influences the stiffness values. That means that elastic deformation is more influenced by anisotropy, while plastic or permanent deformation is influenced more by mineralogy. Also, anisotropy on the microscale in Opalinus Clay is not affected by saturation, contrary to earlier research on the Callovo-Oxfordian shale. The hardness and stiffness of the shaly facies increase much faster with decreasing saturation than the sandy facies. That means that internal and external forces will have a smaller effect on the rock during the open drift stage, but also means that the self-sealing process of swelling, slaking and mechanical closure due to normal stress will decrease, and that repetitive damage by the swelling and shrinking of clay minerals is more severe than in the sandy facies. More research should be done to analyse whether this decrease in self-sealing processes activity will stay after repository closure when resaturation occurs.

8 Acknowledgements

I would like to thank Dr. Martin Ziegler for offering me this master thesis, his efforts and the help he offered me before coming to Zurich, as well as the time he made for me during my time in Zurich. I appreciate the freedom I had and the opportunity to learn so much. Thank you to Jan Rothe for helping with the ordering and the assembling of the climate-controlled boxes. I would also like to thank Dr. André Niemeijer for his help and the discussions we had in Utrecht, as well as the feedback I gained during my time in Zurich. Finally I would like to thank the people at EMPA - Dr. Jakob Schwiedzrik, Cinzia Peruzzi and Jérémie Bérard for assisting me in creating the test setup and ordering parts. Especially for the fact that during the Covid-19 pandemic, we were allowed to bring the Zwick machine and Setaram Wetsys humidity generator to Zurich. That was of extreme importance for this research project, and it is greatly appreciated.

References

Auvray, C., Lafrance, N., and Bartier, D. (2017). Elastic modulus of claystone evaluated by nano-/micro-indentation tests and meso-compression tests. *Journal of Rock Mechanics and Geotechnical Engineering*, 9(1):84–91.

Azhar, M. U., Zhou, H., Yang, F., Younis, A., Lu, X., Fang, H., and Geng, Y. (2020). Water-induced softening behavior of clay-rich sandstone in lanzhou water supply project, china. *Journal of Rock Mechanics and Geotechnical Engineering*.

Blasi, H.-R. (1987). Lithostratigraphie und korrelation der doggersedimente in den bohrungen weiach, riniken and schafisheim. *Eclogae Geologicae Helvetiae*, 80(2):415–430.

Bock, H. (2001). Mont terri rock laboratory. ra experiment, rock mechanics analyses and synthesis, data report on rock mechanics. Technical report, Technical Report TR 2000-02. Federal Office of Water and Geology, Berne.

Bock, H., Dehandschutter, B., Martin, C. D., Mazurek, M., De Haller, A., Skoczylas, F., and Davy, C. (2010). Self-sealing of fractures in argillaceous formations in the context of geological disposal of radioactive waste.

Bossart, P. (2011). Characteristics of the opalinus clay at mont terri. *Mont Terri Project, Wabern Switzerland*.

Bossart, P., Bernier, F., Birkholzer, J., Bruggeman, C., Connolly, P., Dewonck, S., Fukaya, M., Herfort, M., Jensen, M., Matray, J.-M., et al. (2018). Mont terri rock laboratory, 20 years of research: introduction, site characteristics and overview of experiments. In *Mont Terri Rock Laboratory, 20 Years*, pages 3–22. Springer.

Bossart, P., Trick, T., Meier, P. M., and Mayor, J.-C. (2004). Structural and hydrogeological characterisation of the excavation-disturbed zone in the opalinus clay (mont terri project, switzerland). *Applied clay science*, 26(1-4):429–448.

Bossart, P. J., Project, M. T., and fédéral de topographie, S. O. (2008). *Mont Terri Rock Laboratory Project: Programme 1996 to 2007 and Results*. Federal Office of Topography Swisstopo.

Broitman, E. (2017). Indentation hardness measurements at macro-, micro-, and nanoscale: a critical overview. *Tribology Letters*, 65(1):23.

Brown, E. T. (1981). *Rock characterization testing and monitoring*. Number BOOK. Pergamon press.

Charpentier, D., Cathelineau, M., Mosser-Ruck, R., and Bruno, G. (2001). Evolution minéralogique des argilites en zone sous-saturée oxydée: exemple des parois du tunnel de tournemire (aveyron, france). *Comptes Rendus de l'Académie des Sciences-Series IIA-Earth and Planetary Science*, 332(10):601–607.

Chiarelli, A.-S., Shao, J.-F., and Hoteit, N. (2003). Modeling of elastoplastic damage behavior of a claystone. *International Journal of plasticity*, 19(1):23–45.

Delage, P., Le, T.-T., Tang, A.-M., Cui, Y.-J., and Li, X.-L. (2007). Suction effects in deep boom clay block samples. *Géotechnique*, 57(2):239–244.

E92-16, A. (2016). Standard test methods for vickers hardness and knoop hardness of metallic materials.

Fischer-Cripps, A. C. and Nicholson, D. (2004). Nanoindentation. mechanical engineering series. *Appl. Mech. Rev.*, 57(2):B12–B12.

Hostettler, B., Reisdorf, A. G., Jaeggi, D., Deplazes, G., Bläsi, H., Morard, A., Feist-Burkhardt, S., Waltschew, A., Dietze, V., and Menkveld-Gfeller, U. (2018). Litho-and biostratigraphy of the opalinus clay and bounding formations in the mont terri rock laboratory (switzerland). In *Mont Terri Rock Laboratory, 20 Years*, pages 23–39. Springer.

Houben, M., Desbois, G., and Urai, J. (2013). Pore morphology and distribution in the shaly facies of opalinus clay (mont terri, switzerland): Insights from representative 2d bib–sem investigations on mm to nm scale. *Applied Clay Science*, 71:82–97.

ISO-Standards (2005). Iso 6507-1 metallic materials—vickers hardness test-part 1: Test method.

Keller, L. M., Schwiedrzik, J. J., Gasser, P., and Michler, J. (2017). Understanding anisotropic mechanical properties of shales at different length scales: In situ micropillar compression combined with finite element calculations. *Journal of Geophysical Research: Solid Earth*, 122(8):5945–5955.

Knoop, F., Peters, C. G., and Emerson, W. B. (1939). A sensitive pyramidal-diamond tool for indentation measurements. *Journal of Research of the National Bureau of standards*, 23(1):39–61.

Lips, E. and Sack, J. (1936). A hardness tester for microscopical objects. *Nature*, 138(3486):328.

Mäder, U., Waber, H., and Gautschi, A. (2014). New method for porewater extraction from claystone and determination of transport properties with results for opalinus clay (switzerland). In *Proceedings of the 11th International Symposium on Water-Rock Interaction, WRI*, volume 11, pages 445–448.

Marschall, P., Giger, S., De La Vassière, R., Shao, H., Leung, H., Nussbaum, C., Trick, T., Lanyon, B., Senger, R., Lisjak, A., et al. (2018). Hydro-mechanical evolution of the edz as transport path for radionuclides and gas: insights from the mont terri rock laboratory (switzerland). In *Mont Terri Rock Laboratory, 20 Years*, pages 175–196. Springer.

Michalopoulos, Lex, P. and Triandafilidis, George, E. (1976). Influence of water on hardness, strength and compressibility of rock. *Bulletin of the Association of Engineering Geologists*, 13(1):1–22.

Mitchell, J. (1993). Fundamentals of soil behaviour. 2nd edn, 1993.

Niandou, H. (1994). *Etude du comportement rhéologique et modélisation de l'argilité de tournemire: Applications à la stabilité d'ouvrages souterrains*. PhD thesis, Lille 1.

Niandou, H., Shao, J., Henry, J., and Fourmaintraux, D. (1997). Laboratory investigation of the mechanical behaviour of tournemire shale. *International Journal of Rock Mechanics and Mining Sciences*, 34(1):3–16.

Nüesch, R. (1991). *Das mechanische Verhalten von Opalinuston*. PhD thesis, ETH Zurich.

Nussbaum, C., Kloppenburg, A., Caër, T., and Bossart, P. (2018). Tectonic evolution around the mont terri rock laboratory, northwestern swiss jura: constraints from kinematic forward modelling. In *Mont Terri Rock Laboratory, 20 Years*, pages 41–68. Springer.

Ojo, O. and Brook, N. (1990). The effect of moisture on some mechanical properties of rock. *Mining Science and Technology*, 10(2):145–156.

Oliver, W. C. and Pharr, G. M. (1992). An improved technique for determining hardness and elastic modulus using load and displacement sensing indentation experiments. *Journal of materials research*, 7(6):1564–1583.

Peterson, R. W. (1988). Interpretation of triaxial compression test results on partially saturated soils. In *Advanced Triaxial Testing of Soil and Rock*. ASTM International.

Phani, P. S. and Oliver, W. (2019). A critical assessment of the effect of indentation spacing on the measurement of hardness and modulus using instrumented indentation testing. *Materials & Design*, 164:107563.

Ping, C., Qiang, H., Tianshou, M., and Dong, L. (2015). The mechanical properties of shale based on micro-indentation test. *Petroleum exploration and development*, 42(5):723–732.

Savoye, S., Michelot, J.-L., Altinier, M., and Lemius, S. (2008). Origin of pore-water isotopic anomalies near fractures in the tournemire shales. *Physics and Chemistry of the Earth, Parts A/B/C*, 33:S87–S94.

Schmitt, L., Forsans, T., and Santarelli, F. (1994). Shale testing and capillary phenomena. 31(5):411–427.

Smith, R. L. and Sandly, G. (1922). An accurate method of determining the hardness of metals, with particular reference to those of a high degree of hardness. *Proceedings of the Institution of Mechanical Engineers*, 102(1):623–641.

Sone, H. and Zoback, M. D. (2013). Mechanical properties of shale-gas reservoir rocks—part 2: Ductile creep, brittle strength, and their relation to the elastic modulus. *Geophysics*, 78(5):D393–D402.

Tinseau, E., Bartier, D., Hassouta, L., Devol-Brown, I., and Stammose, D. (2006). Mineralogical characterization of the tournemire argillite after in situ interaction with concretes. *Waste Management*, 26(7):789–800.

Tsang, C.-F., Barnichon, J., Birkholzer, J., Li, X. L., Liu, H., and Sillen, X. (2012). Coupled thermo-hydro-mechanical processes in the near field of a high-level radioactive waste repository in clay formations. *International Journal of Rock Mechanics and Mining Sciences*, 49:31–44.

Tsang, C.-F., Bernier, F., and Davies, C. (2005). Geohydromechanical processes in the excavation damaged zone in crystalline rock, rock salt, and indurated and plastic clays—in the context of radioactive waste disposal. *International Journal of Rock Mechanics and Mining Sciences*, 42(1):109–125.

Van Genuchten, M. T. (1980). A closed-form equation for predicting the hydraulic conductivity of unsaturated soils. *Soil science society of America journal*, 44(5):892–898.

Wild, K. M., Wymann, L. P., Zimmer, S., Thoeny, R., and Amann, F. (2015). Water retention characteristics and state-dependent mechanical and petro-physical properties of a clay shale. *Rock Mechanics and Rock Engineering*, 48(2):427–439.

Williams, M., Ziegler, M., and Loew, S. (2019). Mont terri se-p project: Selfsealing in old excavation damaged zones at the mont terri url. Technical report, ETH Zurich.

Wong, R. and Wang, E. (1997). Three-dimensional anisotropic swelling model for clay shale—a fabric approach. *International Journal of Rock Mechanics and Mining Sciences*, 34(2):187–198.

Young, J. F. (1967). Humidity control in the laboratory using salt solutions—a review. *Journal of Applied Chemistry*, 17(9):241–245.

Zhang, C. and Rothfuchs, T. (2004). Experimental study of the hydro-mechanical behaviour of the callovo-oxfordian argillite. *Applied Clay Science*, 26(1-4):325–336.

Zhang, F., Xie, S., Hu, D., Shao, J.-F., and Gatmiri, B. (2012). Effect of water content and structural anisotropy on mechanical property of claystone. *Applied Clay Science*, 69:79–86.

A Matlab code for calculating of the modulus of the sandy perpendicular tetsts

```
clc
clear

Vi = 0.07 %poisson's ratio indenter
Ei = 1141*10^9 %modulus indenter
Vs = 0.22       %poisson's ratio

hcmax15 = importdata ('max_depth_15SL.txt') %import the maximum depth of each test which was exported in another file

%This is a calculation of the reduced and indenation modulus for just the 13% samples. This was done for all saturation levels but were excluded from this appendix for readability and length purposes.
for i=1:1:89
    data = readmatrix(['15%SLHVT (',num2str(i),').csv']); %read the data file of 89 tests

    y = data(:,7); %extract indentation depth data
    x = data(:,2); %extract force data

   plot(x,y,'r') %plot force against indentation depth

    hold on
    title ('15% Saturation')
    xlabel ('Indentation depth [\mum]')
    ylabel ('Force [N]')

    %The following part of the code is from the Master thesis of Fiona Nageli. Here one point is taken where the depth of the indenter starts to decrease, and another point on the curve at 90% of the maximum load.

       y_max=max(y);
     x_max=max(x(y==y_max));

    if x_max<=15;
                x_max2=x_max-0.01*x_max;        %define x_max2 dependent on the indentation depth
    elseif 15<=x_max<=80;                       %area, where slope can be fitted should be low, else, slope goes in wrong direction
                x_max2=x_max-0.05*x_max;
    else
                x_max2=x_max-0.5*x_max;
    end

```

```
    xnew= x(x>= x_max2);        %define xnew, with values above
       x_max2, slope only at these data points

    x1=max(xnew);
    y1=max(y(x==x1));
    ynew=y(x>=x_max2);
    y2=y1*0.9;                          % tell at which position
       the lower point should be (90% of maximum)
    dist    = abs(ynew - y2);           % calculate distance
       between y2 and ynew data
    minDist = min(dist);                % choose the minimal
       distance between y2 and the ynew data
    idx     = ynew(dist == minDist);    % find the ynew value with
        the smallest distance to y2
    y2=max(idx);
    x2=max(x(y==y2));

    A = [x1 x2];
    B = [y1 y2];

    plot(A,B,'*')
    %axis([0 10 0 10])
    hold on
    line(A,B)                             %plots line between the
       two poins, can then be used to calculate the slope
    hold on
    slope15(i) = diff(B)./(diff(A)/10^6);
         %This is the end of the part of the code developed by
            Fiona N{a}geli

    %Based on a Matlab answers post from John D'Errico. This part
       takes the line that was just created and extends it beyond
       the x-axis
pto1 = [x1 y1];
pto2 = [x2 y2];
% A vector along the ray from pto1 to pto2...
V = pto2 - pto1;
factor_distance = 11; %extension factor
pext = pto1 + V*factor_distance; %extension of the line by the
   extension factor
% plot
extended_line = plot([pto1(1),pto2(1)],[pto1(2),pto2(2)],'bo',[
   pto1(1),pext(1)],[pto1(2),pext(2)],'r-') %draw new line until
   it reaches the x axis


coefficients = polyfit([x1,x2], [y1,y2], 1)
a = coefficients (1) %direction coefficient
b = coefficients (2) %intersection y axis

y3 = b
```

```
x3 = 0

x = [x1 x3]
y = [y1 y3]

dy = diff([0 y]);
dyix = find(dy == 0);
y(dyix) = y(dyix-1)+1E-8;
xint15(i) = interp1(y, x, 0); %intersection between the line and
   the x-axis. This is Hr in equation 4.
    end
grid on
axis([0 150 0 15])

%save ('unloading_slope.mat','slope15')

for i = 1:1:89
   hc(i) = hcmax15(i)- (0.9*(hcmax15(i)-xint15(i))); %eq.
      8.2.1.2.3b Fischer-Cripps. Equation 4 in thesis
   hcr(i)= hc(i) /10^6
      Surface15(i) = 24.5* hcr(i)^2; %equation 3
end

save ('unloading_slope.mat','slope99')



for i=1:1:89
   Er15(i) = ((sqrt(pi)/2)*(slope15(i)/sqrt(Surface15(i))))/10^9;
      %reduced modulus
   Eit15(i) = ((1-Vs^2)/((1/(Er15(i)*10^9))-(1-Vi^2)/Ei))/10^9; %
      Fischer crips; %indentation modulus
end

%from here the code for all saturation levels is used
Er15T = Er15'   %transposing values of reduced modulus
Er45T = Er45'
Er60T = Er60'
Er75T = Er75'
Er85T = Er85'
Er99T = Er99'

Eit15T = Eit15' %transposing values of indentation modulus
Eit45T = Eit45'
Eit60T = Eit60'
Eit75T = Eit75'
Eit85T = Eit85'
Eit99T = Eit99'

Ertotal = [Er15T; Er45T; Er60T; Er75T; Er85T; Er99T]; %creating
   one array with all values of Er
```

```
122 Eitotal = [Eit15T; Eit45T; Eit60T; Eit75T; Eit85T; Eit99T]; %
    Creating one array with all values of Eit
123
124 M15 = median(Er15T) %calculation of median
125 M45 = median(Er45T)
126 M60 = median(Er60T)
127 M75 = median(Er75T)
128 M85 = median(Er85T)
129 M99 = median(Er99T)
130
131 M15it = median(Eit15T)
132 M45it = median(Eit45T)
133 M60it = median(Eit60T)
134 M75it = median(Eit75T)
135 M85it = median(Eit85T)
136 M99it = median(Eit99T)
137
138 RH2 = [13 45 60 76 85 99]
139 RH = RH2'
140
141 g1 = repmat({'15%'},89,1); %creating an array with n cells with
    the name '15%', where n is the amount of tests
142 g2 = repmat({'45%'},84,1);
143 g3 = repmat({'60%'},81,1);
144 g4 = repmat({'75%'},89,1);
145 g5 = repmat({'85%'},89,1);
146 g6 = repmat({'99%'},83,1);
147
148 g = [g1; g2; g3; g4; g5; g6]; % One array with all values of g
149
150 Mit = [M15it; M45it; M60it; M75it; M85it; M99it]
151 Mr = [M15; M45; M60; M75; M85; M99]
152
153 figure(2)
154 subplot(2,1,1)
155 boxplot(Ertotal, g, 'notch', 'on', 'positions', RH) %using "g"
    because arrays have different lengths
156 hold on
157 %grid on
158 f = fit(RH, Mr, 'poly2') %quadratic fit creation
159 plot(f, RH, Mr) %quadratic fit plot
160
161 ylabel ('Reduced modulus [Gpa]')
162 xlabel ('Saturation level [%]')
163 axis ([0 105 0 35])
164 legend ('hide')
165 %title('Boxplot reduced modulus Sandy facies parallel to bedding')
166
167 subplot(2,1,2)
168 boxplot(Eittotal, g, 'notch', 'on', 'positions', RH)
```

```
169 %title('Boxplot Indentation modulus Sandy facies Parallel to
       bedding')
170 hold on
171
172 f = fit(RH, Mit, 'poly2')
173 plot(f, RH, Mit)
174 ylabel ('Indentation modulus [Gpa]')
175 xlabel ('Saturation level [%]')
176 axis ([0 105 0 35])
177 legend ('hide')
178
179 medianrsave = [M15; M45; M60; M75; M85; M99]
180 save('MedianErSandyL.txt','medianrsave','-ascii') %this is used
       for the median plots
181
182 medianitsave = [M15it; M45it; M60it; M75it; M85it; M99it]
183 save('MedianEitSandyL.txt','medianitsave','-ascii')
```